

Large-scale structure evolution and sound emission in high-speed jets: real-time visualization with simultaneous acoustic measurements

By JAMES I. HILEMAN, BRIAN S. THUROW,
EDGAR J. CARABALLO AND MO SAMIMY†

Gas Dynamics and Turbulence Laboratory, The Ohio State University, Columbus OH 43235-7531, USA

(Received 20 April 2004 and in revised form 16 June 2005)

This investigation presents a unique and elaborate set of experiments relating the generation of noise to the evolution of large-scale turbulence structures within an ideally expanded, Mach 1.28, high-Reynolds-number (1.03×10^6) jet. The results appear to indicate many similarities between the noise generation processes of high-speed low-Reynolds-number and high-speed high-Reynolds-number jets. Similar to the rapid changes observed in the region of noise generation in low-Reynolds-number jets in previous experimental and computational work, a series of robust flow features formed approximately one convective time scale before noise emission and then rapidly disintegrated shortly before the estimated moment of noise emission. Coincident with the disintegration, a positive image intensity fluctuation formed at the jet centreline in a region that is immediately past the end of the potential core. This indicates mixed fluid had reached the jet core. These results are consistent with the formation of large-scale structures within the shear layer, which entrain ambient air into the jet, and their eventual interaction and disintegration apparently result in noise generation. These results are quite different from the evolution of the jet during prolonged periods that lacked significant sound emission. The observations presented in this work were made through the use of well-established techniques that were brought together in an unconventional fashion. The sources of large-amplitude sound waves were estimated in time and three-dimensional space using a novel microphone array/beamforming algorithm while the noise-generation region of the mixing layer was simultaneously visualized on two orthogonal planes (one of which was temporally resolved). The flow images were conditionally sampled based on whether or not a sound wave was created within the region of the flow while it was being imaged and a series of images was compiled that was roughly phase-locked onto the moment of sound emission. Another set of images was gathered based on a lack of sound waves reaching the microphone array over several convective time scales. Proper orthogonal decomposition (POD) was then used to create a basis for the flow images and this basis was used to reconstruct the evolution of the jet.

1. Introduction

Since the advent of the jet engine and its subsequent use in commercial air travel, a significant amount of work has been devoted to turbulence-generated sound.

† Author to whom correspondence should be addressed: Samimy.1@osu.edu.

Lighthill (1952) made the first significant contribution to our understanding of how sound is produced by turbulence through a reformulation of the governing equations of fluid dynamics into a form analogous to the wave equation. New thinking about turbulence-generated sound appeared after the pioneering flow-visualization work of Crow & Champagne (1971) and Brown & Roshko (1974) established the significance of organized large-scale turbulence structures in free shear flows. In one such work on high-speed low-Reynolds-number jets, Morrison & McLaughlin (1979) found that the region of maximum sound emission coincides with the destruction of the dominant shear-layer instability wave (large-scale coherent structures). The work presented here sheds new light on turbulence-generated sound in high-Reynolds-number jets by combining well-established techniques (flow visualization, proper orthogonal decomposition, acoustic beam forming) that relate the evolution of large-scale turbulence structures to the emission of sound. It does so with a unique experimental set-up and an unconventional means of conditionally imaging the flow during either the emission of sound waves or periods that lacked such emission. Through these methods, findings similar to those of Morrison & McLaughlin (1979) were observed in a high-Reynolds-number jet.

Beyond establishing the importance of large-scale structures to shear-layer development, flow visualization has been used extensively to study their properties. Taking high-speed movies of low-speed jets, both Hussain & Clark (1981) and Hernan & Jimenez (1982) showed how large structures interact through whole and partial pairing. Through the use of flow visualization, Samimy, Zaman & Reeder (1993) and Zaman, Reeder & Samimy (1994) proved the presence of large-scale streamwise vortices in delta-tab modified high-speed jets. In Hileman & Samimy (2003), similar flow-visualization techniques showed delta tabs also regulate the production of large-scale spanwise vortices. In addition, flow visualization has been extensively used to characterize the convective velocity of large-scale structures and the compressibility effects within shear flows (e.g. Brown & Roshko 1974; Papamoschou & Roshko 1988; Murakami & Papamoschou 2000; Thurow, Samimy & Lempert 2003). Various workers have referred to the large coherent structures within a flow as: large-scale structures; large vortices; large eddies; coherent structures; etc. In this work, the term large structure or large-scale structure will be used.

In addition to being the dominant feature of free shear layers, large-scale turbulence structures have a significant impact on noise generation. Owing to the convection of large structures with respect to the ambient, the dominant jet noise radiates at shallow angles ($\theta \sim 30^\circ$) relative to the jet axis (Ffowcs Williams 1963; Lilley 1991). The acoustic field in this direction has a relatively narrow frequency distribution ($St_D \sim 0.1$ to 0.5) (Tam 1991; Simonich *et al.* 2001; Hileman & Samimy 2001). The most intense jet noise originates from a region near the end of the potential core (Fisher, Harper-Bourne & Glegg 1977; Morrison & McLaughlin 1979; Schaffar 1979; Simonich *et al.* 2001; Narayanan, Barber & Polak 2002; Venkatesh, Polak & Narayanan 2003). In their study of low-Reynolds-number jets, Morrison & McLaughlin (1979) attributed the noise-generation process near the end of the potential core to a rapid decay (disintegration) of the dominant instability waves involving a 'relatively violent fluid dynamic action' that could be attributed to a vortex interaction. Freund (2001) used direct numerical simulation to compute the radiating portion of the Lighthill stress tensor in a low-Reynolds-number Mach 0.9 jet, which had been experimentally studied by Stromberg, McLaughlin & Troutt (1980). He found this region of the jet coincided with neither the whole Lighthill source nor with the mean turbulent kinetic energy. Instead, it coincides with the region where the Lighthill sources are

both strong and changing rapidly, and this region is near the end of the potential core. Sarohia & Massier (1977) examined excited subsonic jets with Mach numbers ranging from 0.1 to 0.9 (Re up to 10^6). They found large instantaneous pressure pulses were formed whenever two large-scale structures merged; however, the passage of a large structure did not significantly change the near-field pressure signal. The overall conclusion of these works is that acoustic radiation results from the dynamic interplay of the large-scale structures within the jet's shear layer (their interactions lead to production of Reynolds stresses, which are the source of acoustic radiation in Lighthill's acoustic analogy). Hence, a key part of understanding the production of turbulence mixing noise lies in determining the large-scale structure dynamics that lead to noise production (Crighton 1975). This work examines the time evolution of large-scale structures during the creation of intense sound waves (as well as prolonged periods lacking such sound emission). Since the acoustic radiation due to large structures is at angles shallow to the jet and the source of their radiation is from a region surrounding the potential core, the microphone array of this work was placed at a shallow angle and the flow images were taken of a region surrounding the end of the potential core.

This work is a continuation of Hileman & Samimy (2001) and Hileman, Thurow & Samimy (2002) where microphone array measurements were used with flow visualization to relate the emission of sound to the evolution of large-scale turbulence structures within a high-Reynolds-number ideally expanded Mach 1.28 jet. This work improves on these earlier studies by incorporating a three-dimensional microphone array to locate sound sources, two orthogonal flow-visualization systems to capture three dimensions of the evolution of the large-scale structures, and analysis of the flow images with proper orthogonal decomposition (POD). Other workers have conducted experiments using simultaneous point measurements of the flow and acoustic fields (e.g. Lee & Ribner 1972; Siddon 1973; Sarohia & Massier 1977; Morrison & McLaughlin 1979; Schaffar 1979; Panda & Seasholtz 2002). This and our earlier work mentioned at the beginning of this paragraph are the first to use a noise source location technique with any form of planar flow measurement. Further, both of these techniques were non-intrusive, which is not the case for most previous analyses. The use of planar visualization should significantly assist the examination of noise sources, which are distributed in nature. In addition to this unique aspect, these works represent the first attempts to make a distinction between the evolution of large-scale structures during periods when sound is being generated and periods that lack such acoustic radiation. By understanding the differences between these two different 'states' of the jet, we should gain a more fundamental understanding of the large-scale structure evolution and dynamics that are important to the generation of sound.

2. Experimental arrangement and techniques

2.1. Facility

All of the experiments were conducted in the optically accessed anechoic chamber of the Gas Dynamics and Turbulence Laboratory of The Ohio State University. This facility is equipped for flow measurements via optical diagnostics in a fully anechoic environment. The inner dimensions of the chamber, from wedge tip to wedge tip, are 3.1 m in width and length, and 2.7 m in height. Additional details of the anechoic chamber, its validation and the jet facility can be found in Kerechanin, Samimy & Kim (2001), Hileman & Samimy (2001) and Hileman (2004). The jet nozzle had an exit diameter, D , of 25.4 mm and a 2.5 mm lip thickness. The exit Mach number was

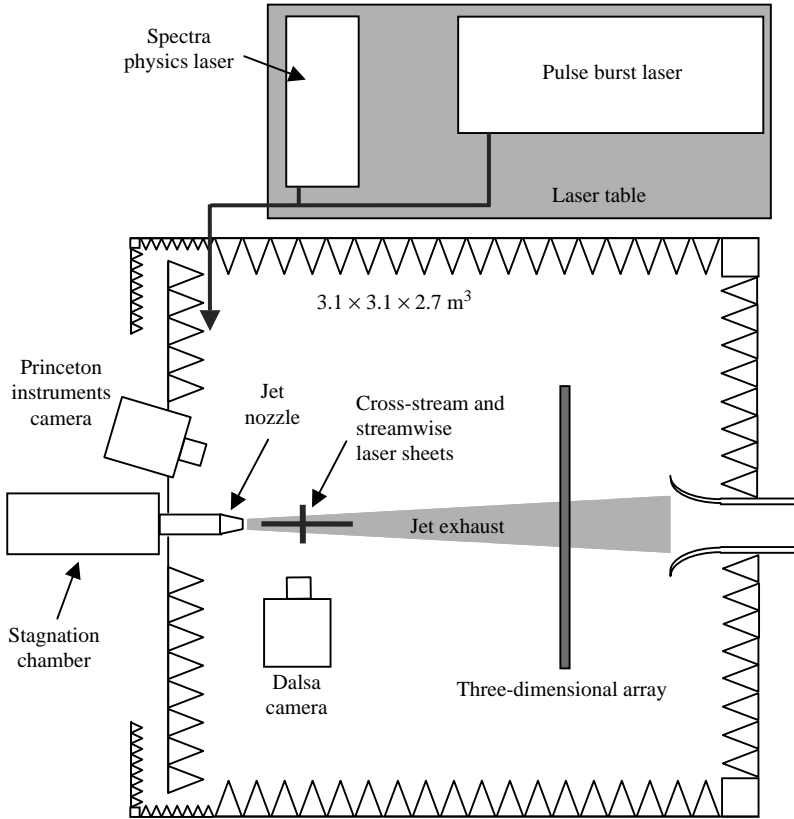


FIGURE 1. Schematic of the jet within the anechoic chamber and the equipment used in the simultaneous flow/acoustic experiments. Figure is not to scale.

measured as 1.28 with a calculated exit velocity of 385 m s^{-1} and a Reynolds number of 1.03×10^6 . The convective velocity of the large-scale structures, u_c , was measured as 266 m s^{-1} by Thurow *et al.* (2003). The theoretical convective Mach number, M_c , for the jet was 0.59 using the formula of Papamoschou & Roshko (1988). We used an unheated Mach 1.3 jet to facilitate flow visualization and to achieve a convective Mach number match to a typical jet engine exhaust. For comparison, a Mach 0.9 jet with a stagnation temperature of 800°K has M_c of 0.55. The boundary layer at the nozzle exit is estimated to be turbulent with a boundary-layer thickness of the order of 1 mm. These are inferred from some crude measurements conducted on a Mach 0.9 jet with a similar sized nozzle (Kastner, Hileman & Samimy 2004). To fully characterize the boundary layer, we must obtain a large number of measurements within this 1 mm thickness, which is unattainable with currently available measurement technology.

The experiments consisted of acoustic source localization in three dimensions and flow visualization in two planes, as shown in figure 1. A large number of realizations consisting of 19 750 simultaneously acquired flow and acoustic data sets were obtained. Each set consisted of a single flow image in the cross-stream plane, 17 temporally resolved flow images in the streamwise plane (at 167 kHz rate), and 8.192 ms of data from the microphone array. For comparison, the convective time scale based on the jet exit diameter and the convective velocity in the jet is about $96 \mu\text{s}$ (most

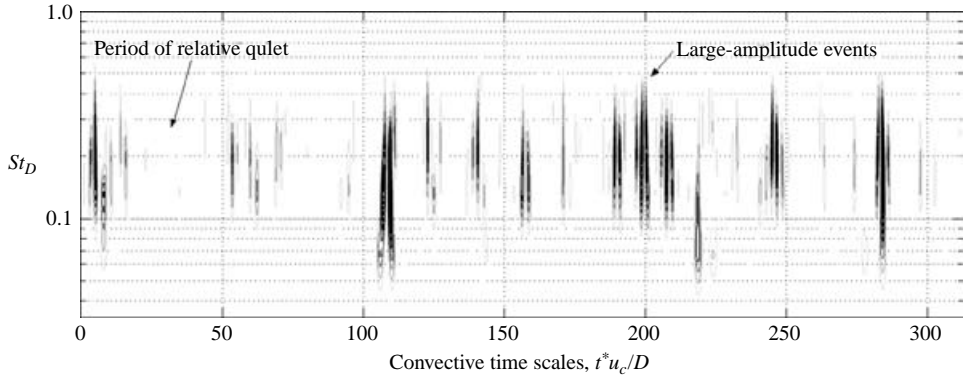


FIGURE 2. Frequency distribution over a short period of time of a typical far-field acoustic data segment (obtained using Mexican hat wavelet) at $\theta = 30^\circ$.

time dimensions have been normalized by this time scale). The large number of realizations was deemed necessary to ensure that a statistically significant number of images were captured during the noise emission process. The laser systems and one of the cameras were located outside the anechoic chamber, while another camera was inside the chamber. Apparent noise source origins were computed in four-dimensional space–time. The next two sections will discuss additional details of these experimental techniques.

2.2. Microphone array

Since the primary purpose of this work is to relate the time-resolved jet structure to the instantaneous emission of sound, acoustic data were analysed largely in the time domain. Figure 2 shows sample jet far-field acoustic data in the time and frequency domains for a microphone at a 30° angle with respect to the jet axis, which is the location of maximum sound emission (Hileman & Samimy 2001). The plot gives 310 convective time scales (30 ms) of acoustic data that has been transformed into the frequency–time domain. The conversion was performed with a Mexican hat wavelet transformation since it bears much similarity to a waveform created from an average of the large-amplitude acoustic events (see Hileman *et al.* 2002; Hileman 2004). The ordinate of this plot is given in terms of Strouhal number (based on jet exit velocity and nozzle exit diameter) while the abscissa is given in terms of convective time scales, t^*u_c/D . The energy distribution mimics the information of the raw signal, but instead of having precise information about the amplitude of the peaks, it gives their frequency. The figure shows ‘large-amplitude events’ (acoustic peaks with amplitude exceeding two standard deviations of the sound pressure fluctuations, σ) being interspersed among prolonged ‘periods of relative quiet’ (periods lacking any peaks exceeding 1.5σ with duration exceeding 5 convective time scales). The Strouhal numbers of the energy distribution match the peaks of the overall acoustic data ($St_D = 0.15$) at this location (Hileman 2004). A novel application of conventional microphone array techniques was used to determine the origin of these ‘large-amplitude acoustic events.’ The frequency of each large-amplitude event was estimated by determining the Mexican hat wavelet width that best matched the acoustic data through an optimization routine. Thus, the magnitude, frequency and apparent source of every large-amplitude event were determined and were then compared to the flow structures in simultaneously acquired flow images. In addition to the easily identifiable large-amplitude temporal acoustic peaks observed in the 30°

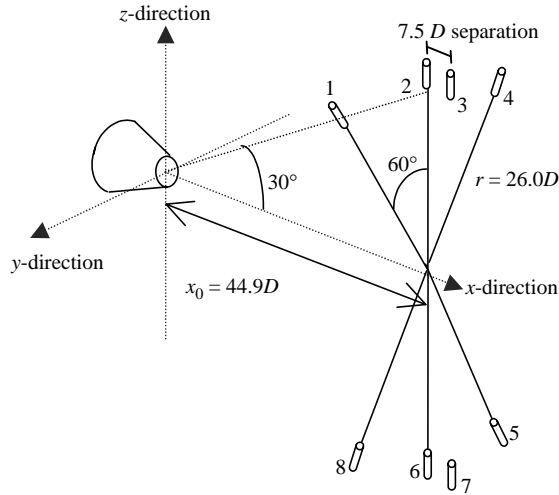


FIGURE 3. Schematic of the three-dimensional microphone array showing the microphone locations relative to the nozzle exit and jet axis.

direction, acoustic radiation in this direction has large coherence over relatively long distances in both the radial and azimuthal directions. This coherence was exploited in the microphone array design.

The microphone array and beamforming algorithm are discussed at length in Hileman, Thurow & Samimy (2004), so only highlights are presented here. The noise source localization relies on measurement of the phase lag of individual large-amplitude acoustic events between microphones in space, using short segments of acoustic data. With this phase-lag information and the geometry of the array, a three-dimensional spatial origin is determined for the large-amplitude acoustic events. The microphone array has a total of eight microphones: six azimuthally distributed to determine the origin in the cross-stream plane and two sets of inline microphones to determine the origin along the jet axis. A large azimuthal coherence (> 0.5) allowed for microphone separations of up to 60° to compute the y - and z -components of the source location. Figure 3 shows a diagram of the array configuration in relation to the jet axis and the nozzle. Owing to problems in the bottom inline microphones (6 and 7) that were only discovered after the data acquisition was complete, the top microphones (1 through 4) were used to compute the x and y components of the noise origin. Microphones 1, 4, 5 and 8 were used to compute the z -location. Data from the top front microphone were used with the spatial source location to determine when the large-amplitude events were created with respect to the flow imaging, thus defining the fourth dimension of space-time noise source localization. To minimize the possible impact of refraction on the source locations, the phase lag for each large-amplitude acoustic event was computed between the top and bottom front microphones (2 and 6). Only events with a positive z -location and corresponding phase lag were considered as being above the jet centreline in §§ 3.3 and 3.4. It should be noted that this array beamforming technique will not work when placed normal to the jet (i.e. $\theta \sim 90^\circ$) because there are no easily identifiable large-amplitude acoustic events and the coherence decreases rapidly over short azimuthal distances at this observation location. These findings were consistent over a range of Mach numbers between 0.9 and 2.0 (Hileman 2004; Hileman *et al.* 2004) and are consistent with a

theory that divides the turbulent mixing noise into two components based on the angular dependence of acoustic radiation (Tam, Golebiowski & Seiner 1996; Tam 1998; Tam & Zaman 2000).

A pulsed plasma arc and a small fluidic device were used to evaluate the microphone array. The plasma arc approximated a point source to test the frequency response while the fluidic device was modified to produce tonal (2.1 or 3.4 kHz tones) as well as broadband (central frequency of 7 kHz) acoustic radiation. The microphone array accurately located the source region of the fluidic device as well as the plasma arc when it was producing acoustic frequencies under 10 kHz ($St_D = 0.65$). For this reason, the acoustic data were low-pass filtered at 10 kHz using a fifth-order Chebyshev type I digital filter. The array and associated beamforming algorithm have also been used to determine the three-dimensional source distribution from an ideally expanded Mach 1.28 jet with one and two delta tabs (Hileman & Samimy 2003) as well as Mach 0.9 and 2.0 jets (Hileman 2004). Further details of the microphone array as well as the timing used to relate the flow and acoustic data can be found in Hileman & Samimy (2001), Hileman (2004) and Hileman *et al.* (2004).

2.3. Flow visualization

The instantaneous state of the jet mixing layer was captured over a two-dimensional plane by a sheet of light created by a high-power pulsed laser. The laser beam pulse width is ~ 10 ns, over which the motion of the fluid is essentially frozen. A digital camera is used to capture the scattered light, which gives a planar image of the jet. Light-scattering particles are formed in the flow naturally through the process of product formation. For the Mach 1.28 jet of the current work, the air temperature of the jet core is approximately -50°C . When ambient air becomes entrained into the jet's mixing layer, moisture condenses into small particles that scatter the light from the laser sheet, thus marking the majority of the mixing layer. The condensed water particles are of the order of 50 to 100 nm, which is smaller than the wavelength of the incident light (532 nm) so the scattering falls somewhere between the Rayleigh and Mie regimes. It should be emphasized that product formation occurs only within the mixing layer of the jet. This is advantageous to the present study since the purpose is to relate the evolution of the large-scale structures within the mixing layer to the emission of sound.

Streamwise and cross-stream images of the mixing layer were simultaneously provided by two separate laser/camera systems. As shown in figure 1, both lasers were located outside the anechoic chamber and their beams were brought into the facility through a small opening in the chamber wall. The two beams were orthogonally polarized. Through the use of two high-energy Nd:YAG laser thin-film polarizers, they travelled along the same path into the chamber. The cross-stream sheet was formed by a conventional Spectra Physics Pro250 Nd:YAG laser operating at 532 nm wavelength and images were captured by a 14 bit Princeton Instruments ICCD camera with a resolution of 576×384 . The streamwise sheet was formed from a home-built pulse-burst Nd:YAG laser and temporally resolved image sets (short duration movies) were acquired at a high frame rate using a camera from Dalsa (model 64K1M ultra-high-speed camera). This system was capable of operating at a MHz rate, but the camera was limited to 17 frames, so the imaging rate was set at 167 kHz to obtain high-quality image sets. Image resolution was 245×245 pixels with 12 bit depth. The pulse-burst laser produces 532 nm wavelength light with a measured output power of 25 mJ pulse for 17 pulses separated by $6 \mu\text{s}$. Details of the pulse-burst laser and high-speed camera can be found in Thurow *et al.* (2002, 2003).

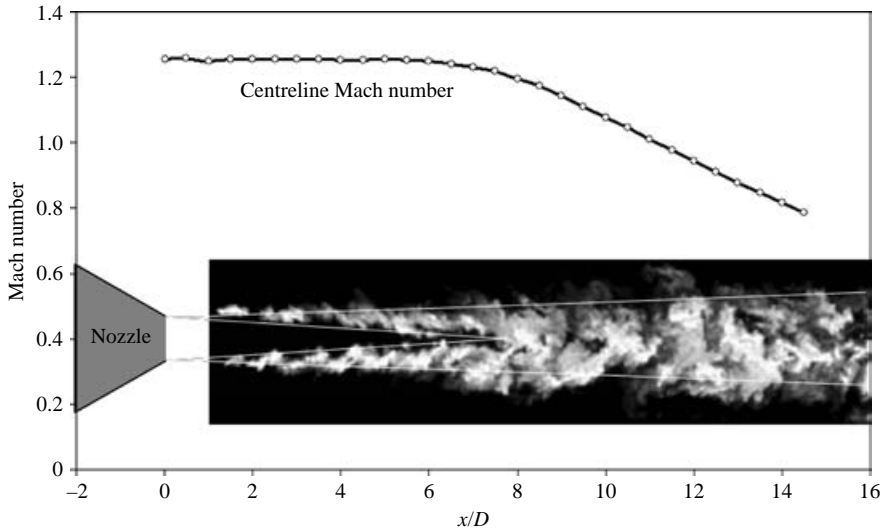


FIGURE 4. A typical jet flow image with measured average centreline Mach number and nozzle schematic. Figure is to scale.

To maximize the likelihood of capturing flow images during the generation of large-amplitude acoustic events, the two orthogonal laser sheets were centred on the mean of the noise source distribution region, which is between 9 and $10x/D$ (shown in § 3.1). The cross-stream image was taken at $9x/D$ while the streamwise images covered a range from 6 to $12x/D$. The cross-stream sheet was created simultaneously with the seventeenth image of the streamwise temporally resolved set of images. Because of contamination from the cross-stream image in the streamwise plane, only the first 16 temporally resolved images were usable and thus the movie duration was $90 \mu\text{s}$.

Figure 4 shows a sample flow image given to scale with a jet nozzle schematic and centreline average Mach number distribution. For this image, the conventional laser was used with a 16 bit PixelVision CCD camera having a resolution of 1024×1024 . Thin white lines within the visualization delineate the average of many such images. The initially thin mixing layer grows until the two sides begin to interact around $6x/D$, which is where the centreline Mach number starts to deviate from 1.28 . The region between the two sides of the mixing layer where the flow is undisturbed represents the jet core. Between 7 and $14x/D$, the jet consists of organized masses of mixed fluid (large structures) that resulted from the merging of the mixing layer. As such, they span the width of the jet. This work will focus on these organized features and their time evolution as captured with flow visualization. A typical instantaneous cross-stream image is shown in figure 5(a) before and in figure (b) after conversion to binary (the binary conversion will be discussed in the next section). An average of many of these images is round with a decreased intensity at the centre and toward the edges of the jet. Figure 6 shows a typical streamwise image (from a set of temporally resolved images) before and after conversion to binary. Figure 6(a) has been modified by the removal of a vertical line at $9x/D$ (caused by the cross-stream laser sheet), digital filtering, and a normalization procedure that brought the intensities of all of the columns to a maximum value of one. Figure 6(b) shows the flow image after conversion to binary. Temporally resolved image sets from the jet used here can be found in Hileman *et al.* (2002), Hileman (2004) and Thurow *et al.* (2002, 2003).

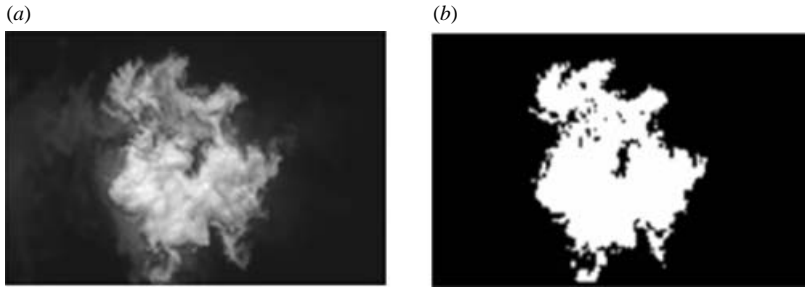


FIGURE 5. (a) A typical cross-stream instantaneous image and (b) the image after conversion to binary. Image acquired at $9x/D$. Binary images were used for statistical and POD analyses.

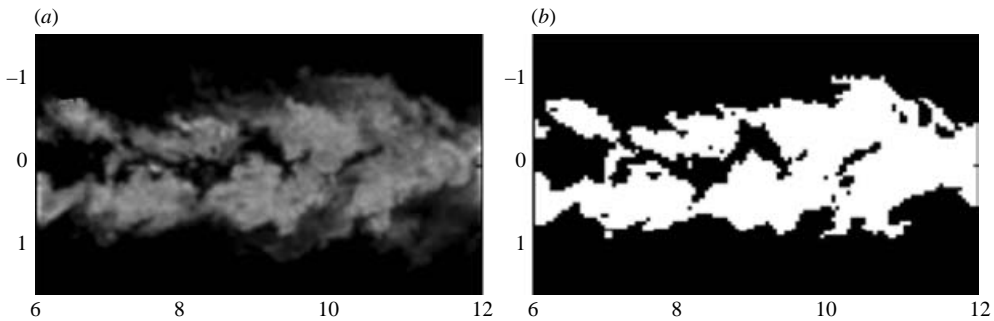


FIGURE 6. (a) A typical streamwise image and (b) the same image converted to binary. Distances are in jet diameters.

2.4. Proper orthogonal decomposition

The flow images of the preceding section were acquired to gain a better understanding of the large-scale structures within the jet. Initially, individual images were examined visually with the intent of uncovering common trends. This type of analysis depends on the examiner's interpretation of what is important within any given flow image. To facilitate an objective analysis of the images, the proper orthogonal decomposition (POD) technique was chosen. POD is also known as the Karhunen–Loeve technique in other areas of study. The technique was introduced to the turbulence community as an objective means of extracting coherent large-scale structures from turbulence data by Lumley (1967). POD has been used extensively to define the most energetic structures/modes in jets. For example, it has been used with data from low-speed jet experiments (e.g. Citriniti & George 2000), high-speed jet experiments (e.g. Ukeiley & Seiner 1998), and high-speed jet simulations (e.g. Freund & Colonius 2002; Caraballo *et al.* 2003). The technique mathematically decomposes a flow field into a set of eigenmodes (referred to as POD modes) that form a basis for the relative size and position of the most energetic flow features (in an average sense). In a sense, the first mode captures the most common deviation from the mean while the second mode captures the most common deviation from the first mode, and so on. These eigenmodes yield a distribution in size and space of the flow features, and multiple modes are generally required to gain a proper representation of the large-scale turbulence structures. The snapshot method of Sirovich (1987) was used for modal creation in this work as it was designed for the analysis of large realizations of highly spatially resolved data, and these are characteristics of the flow images employed here.

The POD of this study used image intensity fluctuations as the working variable, and the technique was optimized for intensity variation. The POD modes were then projected onto select flow images yielding a set of weighting factors which could then be used to reconstruct the jet from a select number of POD modes.

Since the quantity being analysed with POD is image intensity, additional considerations must be made for image processing. This is because the image intensity is affected by other variables that are not directly related to the physical properties of the jet and one or more of these variables could potentially change from one set of images to the next. The intensity of any flow image relies on three main things: the seed particles that mark the flow, the intensity of the light that is scattered by the particles, and the camera that captures the images. In the flow visualizations used in this work, the seed particles were provided by the condensation of humidity within the entrained ambient air that occurred upon mixing with the cold jet air within the mixing layer of the jet. Thus, the seeding of the jet relied on the dew point of the ambient air. Another important factor was laser beam intensity. The amount of power produced by the pulse-burst laser system depended largely on a tedious optimization process. These parameters caused significant variations within flow images taken of the same jet operating at the same stagnation temperature and pressure. Owing to changes in the pulse burst laser power between two of the four days of data acquisition, nearly half of the streamwise image sets were of significantly lesser quality. The change was enough to alter the average image and POD modal shapes. Because of this, only 10 750 of the 19 750 streamwise temporally resolved image sets were used in the analysis (Hileman 2004).

Based on the aforementioned issues, it was deemed unacceptable to allow fluctuations in intensity (other than a simple on-off binary difference) into the POD calculations. Example images before and after conversion to binary were given in figures 5 and 6. The binary images show a region as being mixed (sufficient condensation present) or not mixed (insufficient condensation). The binary-conversion procedure changed slightly, depending on the orientation of the laser sheet (cross-stream or streamwise) and the flow-visualization system used to capture the images. In all cases, however, pixels below a user-defined threshold were ignored, all remaining pixels were normalized by a maximum intensity, and then the image was converted to binary based on a threshold of 0.4. This threshold level set the amount of mixing between the ambient and jet that must be present for an area to be defined as mixed. Various threshold levels were examined and 0.4 was chosen since it gave a well-defined unmixed core and it best preserved the delineation between large-scale structures within the mixing layer. The binary images of figures 5 and 6 show that the conversion process yields a jet core that is well-defined and similar in extent to the original image. The use of binary will invariably lead to the smearing of some features into a single large-scale structure since their boundaries will often be eliminated, but as can also be observed in figures 5 and 6, there is still a demarcation among the large-scale structures that dominate the mixing layer.

3. Experimental results

This work focuses on the relationship between the evolution of large-scale structures within high-speed jets and the production of sound. Section 3.1 of the results confirms existing knowledge through analysis in an average sense where the region of noise generation is determined and then the flow within this region is analysed. The later sections present analysis that goes beyond this approach. In a unique methodology,

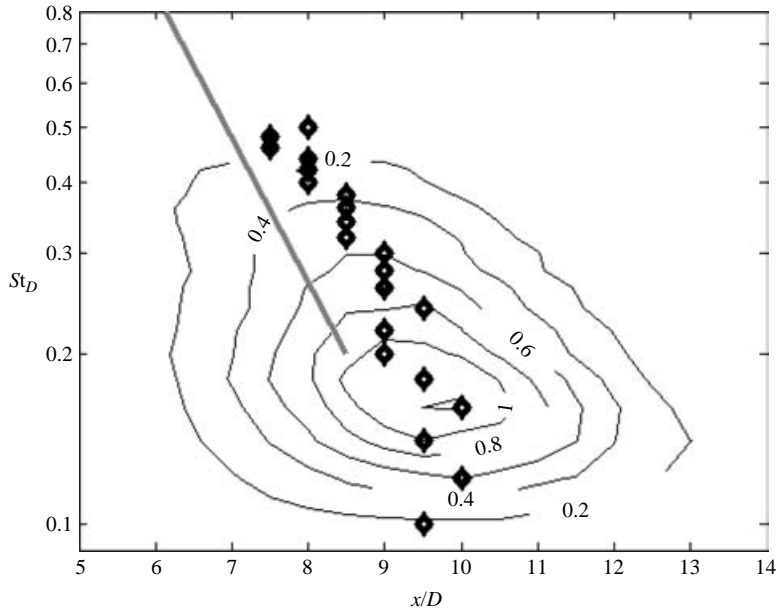


FIGURE 7. Noise source distribution. Contour levels gives percentage of events within each bin and \diamond , centroids give the mean values for each frequency bin. Solid line is from Venkatesh *et al.* (2003) who obtained it from the compilation of established noise source data in literature.

the properties of the mixing layer were compared for two situations: (i) while large-amplitude acoustic events were being produced, and (ii) prolonged periods of relative quiet as recorded by the microphone array. These situations can be thought of as two jet ‘states’. The POD was used to derive mathematical bases of the flow images for further analysis in §3.2. In §3.3, individual images are selected for this analysis using set criteria, i.e. the jet states are formally defined. The unique properties of these two disparate jet states were then determined using image reconstruction from the POD basis in §3.4.

3.1. Mean jet properties

As was discussed in §2.2, the microphone array algorithm of the current study differs from those used in previous works on jet noise. However, the results are consistent with the available literature. The data set analysed by the microphone array consisted of 86.7 s of data that yielded 99 388 acoustic peaks with a magnitude larger than 2.0σ . The mean values for the three spatial coordinates (x_s, y_s, z_s) of this data set were $(9.3 \ 0.0 \ 0.4) D$ with standard deviations of $(1.9 \ 0.3 \ 0.3) D$. The non-zero mean z_s was due to misalignment of the array’s centreline with that of the jet and is small compared with the array diameter ($52.0D$). The mean z_s value was subtracted from the individual noise sources prior to compilation into probability distributions. Figure 7 shows the probability distribution of event Strouhal number as a function of streamwise noise source location. The distribution was computed using a bin size of $0.5x/D$ by $0.05 St_D$. The mean location (centroid) for each of the frequency bins has also been included on the distribution. Figure 8 shows the probability distribution of event magnitude as a function of streamwise noise source location with binning of $0.5x/D$ by 0.05σ . The largest-amplitude acoustic events were created between 8 and $10x/D$ and the peak jet noise for the Mach 1.28 jet ($St_D = 0.15$ at 30°) originated from $\sim 9.5x/D$. These

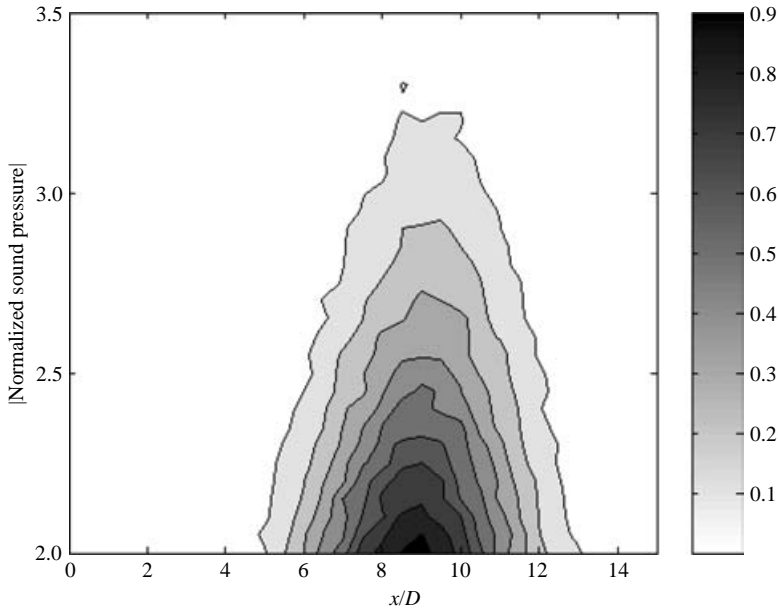


FIGURE 8. Probability distribution of sound pressure magnitude as a function of streamwise noise source location for the jet. Grey scale bar gives percentage of events within each bin.

data connect the peak turbulence mixing noise to a position within the jet, i.e. this is the location of peak noise emission by events related to the large-scale structures. The line within figure 7 shows a fit to existing jet noise source location data that was acquired using a variety of microphone array techniques (Chu, Laufer & Kao 1972; Grosche 1973; Fisher *et al.* 1977; Ahuja, Massey & D'Agostino 1998; Venkatesh *et al.* 2003). These data consisted of both heated and unheated jets that spanned a range of Mach numbers between 0.5 and 0.9. The current data match the trend of the existing data well. The location of the peak noise can be compared to the study conducted on a heated ($T_0 = 810^\circ\text{K}$), Mach 0.9 jet by United Technologies Research Centre (Simonich *et al.* 2001; Narayanan *et al.* 2002; Venkatesh *et al.* 2003). In those works, the jet noise peak at 30° was measured at $St_D = 0.16$ and this frequency had a peak source strength at $8.5D$ with significant radiation from all locations between the nozzle exit and 18 jet diameters. Thus, there is a good match between the source and frequency of the peak jet noise for their heated Mach 0.9 jet and the unheated Mach 1.28 jet of the current study. The approximately one jet diameter difference between the Mach 1.3 noise sources presented here and those of the literature arises from the lengthened potential core of the Mach 1.3 jet over the subsonic jets (Hileman 2004).

The probability distribution of the apparent noise source location for the other two components (the cross-stream distribution) for all streamwise locations is presented in figure 9 with the nozzle lip line shown to scale. This distribution can then be compared to the average flow images of figure 10, which show the development of the jet mixing layer. The figure is comprised of average flow images at 11 cross-stream locations ($1x/D$ increments). Each image was created from 250 instantaneous images. The nozzle exit and jet centreline are given to scale. The mixing layer of the jet starts as a thin ring and it grows into a solid disk. The distribution is symmetric and the centre coincides with that of the jet. Figure 11 provides average streamwise data consisting of the noise source location distribution, the average Mach number

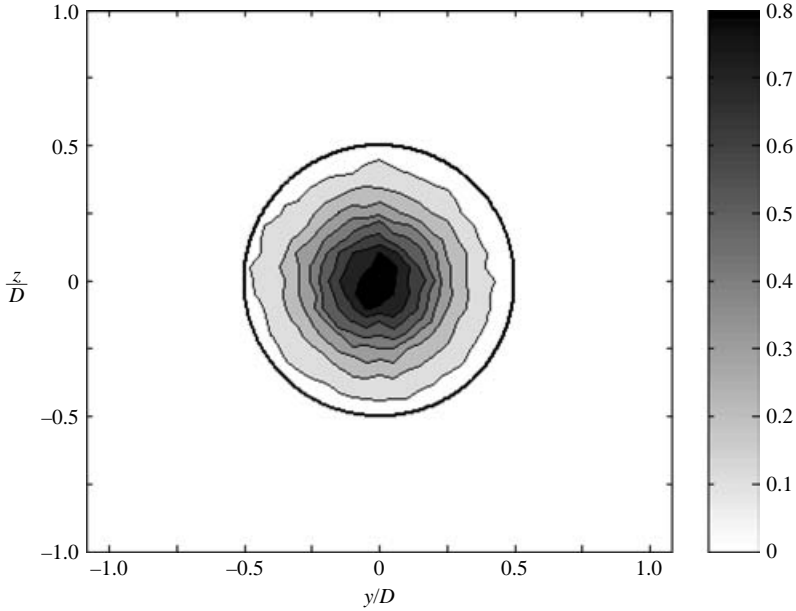


FIGURE 9. Two-dimensional probability distribution of the cross-stream noise source locations (y, z). Nozzle lip-line is drawn to scale. Grey scale bar gives percentage of events within each bin.

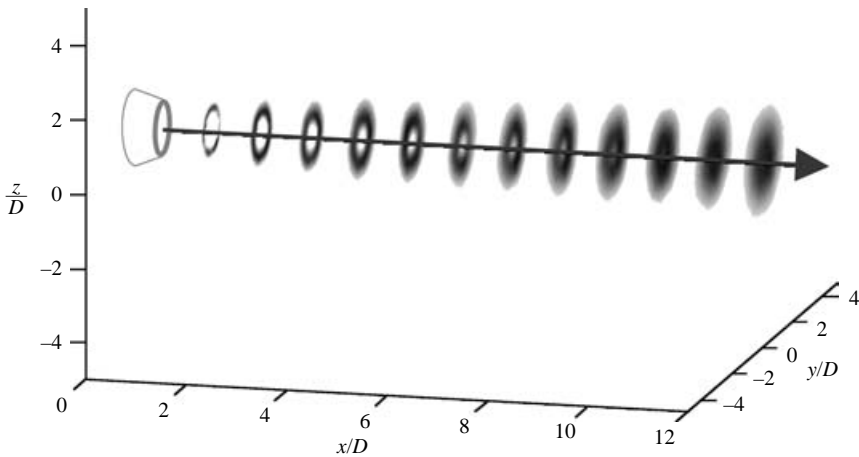


FIGURE 10. Average cross-stream images of the jet between 1 and $12x/D$.

along the jet centreline and the nozzle lip-line, and an average streamwise flow image spanning 1 to $16x/D$ that was created from 500 individual images similar to that of figure 4. This compilation allows for a quick comparison of some average quantities of the jet within the region of maximum noise source concentration. The schematic in the corner of the figure shows the relation of the laser sheet to the two Pitot probe measurement locations. The region of peak noise source concentration coincides with the region where the two sides of the mixing layer have merged in the average flow image, and it is downstream of the end of the potential core as shown by the centreline Mach number plot. Thus, the ellipsoid-shaped region of high noise source

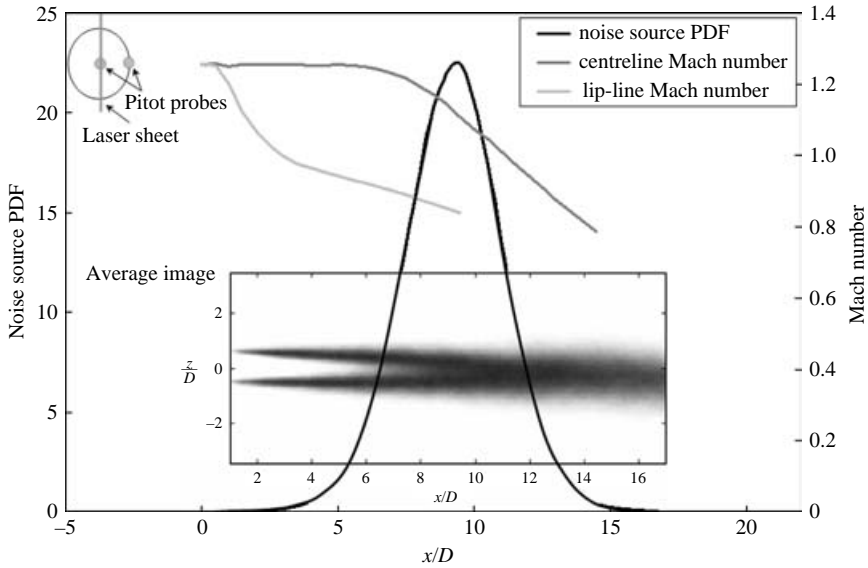


FIGURE 11. Compilation of the jet data. The noise source probability density function (PDF) is given from the left-hand ordinate, the Mach number on the right-hand ordinate, and the average image is to scale. The schematic in the upper left-hand corner shows the location of the Pitot probes and the laser sheet with respect to the jet centreline.

concentration corresponds to the region downstream of the end of the potential core where the mixing layer of the jet becomes a mass of mixed fluid.

3.2. POD modes

Two orthogonal laser sheets (discussed in §2.3) were used to visualize the flow within the ellipsoidal region of high noise source concentration. Using proper orthogonal decomposition (as discussed in §2.4), a basis of POD modes was created from these images that was used in the flow analysis. The working variable was image intensity fluctuation from the mean and the images were converted to binary prior to analysis. The first 24 POD modes were computed for the cross-stream flow images using 2000 of the 19750 acquired images (recall that these were acquired at $9x/D$) and are presented in figure 12. In addition to the 24 cross-stream POD modes, the first 16 streamwise POD modes were computed from the sixth image (of each 17 image set) of 2000 of the 10750 temporally resolved flow image sets. These are presented in figure 13. The POD method was applied to the region between 7 and $11x/D$ to emphasize the area surrounding the maximum noise source concentration. The percentages of the total intensity variance captured in each mode are given in the figures and the greyscale of the images shows positive (white) and negative (black) intensity fluctuations from the mean. The relative sign of the modes is not important among different POD modes, only the relation of the signs within an individual mode matters. The convergence of both sets of modal shapes was examined in Hileman (2004) and the modes had reached convergence with this image set size. However, a few of the higher-order modes changed shape slightly between set sizes of 1500 and 2000 and the addition of more images to the set would probably lead to some small changes in the higher modal shapes. For comparison, while these 2000 images were completely uncorrelated in time, the POD analysis of Freund & Colonius (2002) used 2333 correlated realizations of the flow field.

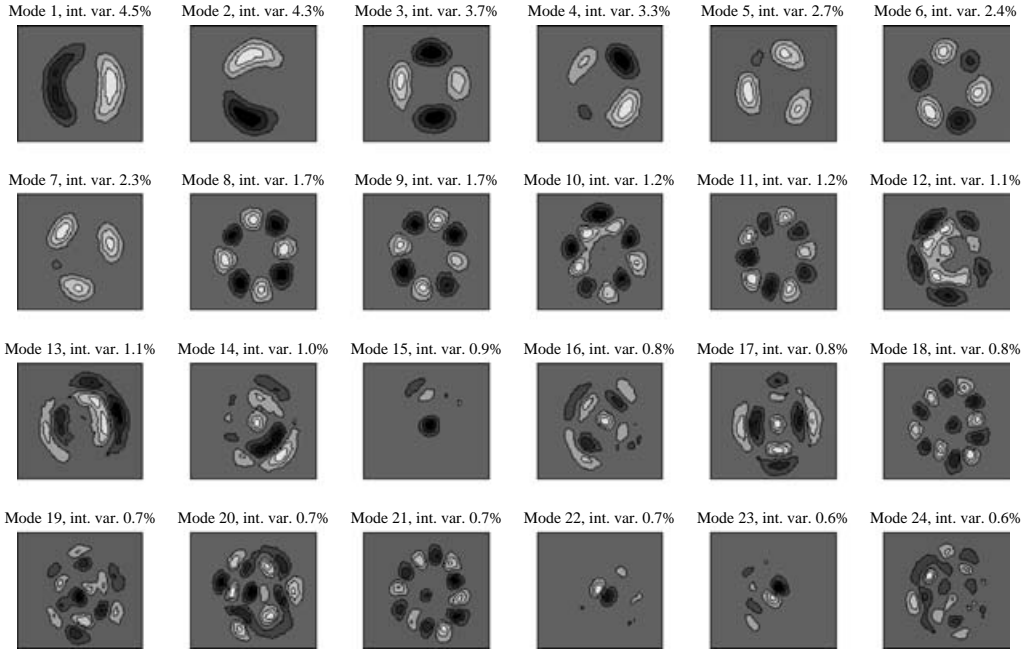


FIGURE 12. POD modes created from 2000 flow images of the cross-stream plane at $9x/D$ using the intensity fluctuations from the mean. White and black show opposite intensity fluctuations.

The cross-stream POD modes of figure 12 can be thought of as a basis that captures the relative size and spatial distribution of the jet’s significant features (i.e. the large-scale turbulence structures). The first 11 modes seem to reflect variations on the outer edge of the jet and these modes occur mostly in pairs, i.e. modes 1 and 2 have two alternating-sign fluid masses, modes 8 and 9 consist of eight masses, and modes 10 and 11 consist of ten masses. These lower-order modes can be expressed in a sinusoidal ($\sin n\phi$) form consistent with a Fourier decomposition where the factor n is the azimuthal mode number and the two similar modes have a 90° phase shift. POD modes 1 and 2 have $n=1$, modes 3 and 4 have $n=2$, modes 8 and 9 have $n=4$ and modes 10 and 11 have $n=5$. The exception to this is POD modes 5 to 7 where only mode 6 follows the previous trend. Modes 5 and 7 largely consist of three positive fluctuations. A likely scenario for this case is a combined axisymmetric mode ($n=0$) with the 90° phase shifted version of mode 6 ($n=3$). When the entire intensity range was used in the modal computation, modes 5 and 6 had $n=3$ while mode 7 was axisymmetric. When 1000 binary images (instead of 2000) were used in the modal computation, mode 5 was largely axisymmetric and modes 6 and 7 had $n=3$. Thus, it seems safe to assume that modes 5 to 7 of figure 12 are a combination of an $n=0$ axisymmetric and $n=3$ azimuthal modes. The higher-order modes (12 to 24) consist of features that span the entire jet and are too complex to be expressed with a simple sinusoidal relationship. Modes 14 to 18 have a clearly defined feature at the jet centre, while modes 22 and 23 have a pair of such features. Mode 15 is unique in that it has a dominant centre feature. Modes 18 and 21 also have alternating-sign flow features (12) around the periphery of the jet, but there is also a feature at the jet centre. A few of the higher-order modes (19, 20 and 24) are quite complex. Even though a large number of modes are computed here, they comprise only 40 %

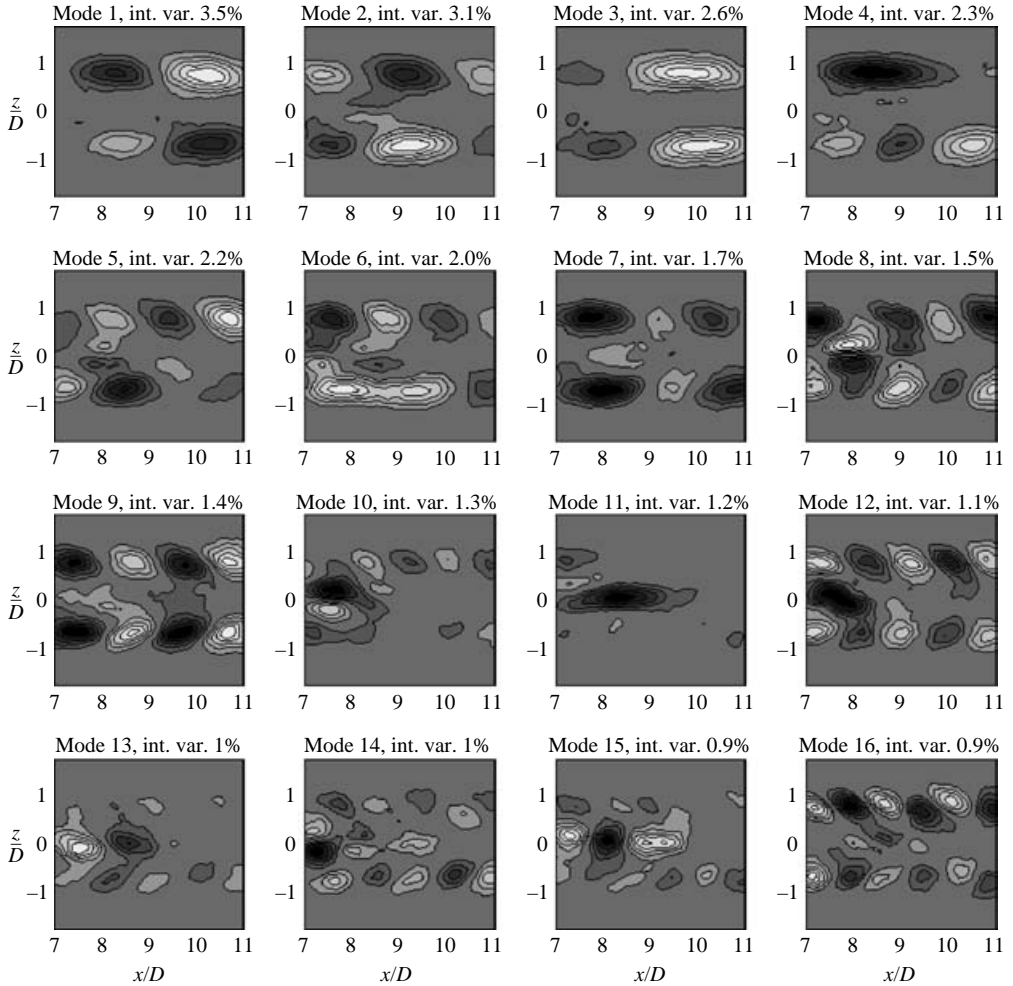


FIGURE 13. POD modes created from 2000 flow images of the streamwise plane between 7 and $11x/D$ using the intensity fluctuations from the mean intensity.

of the total intensity variance. For a POD problem such as this (involving image intensity), we must have a large number of modes to capture all of the intensity variance. However, the distribution of the significant aspects of the mixing layer (the large-scale turbulence structures) should be captured, as evidenced by the decreasing size of the flow features that are within higher-order modes.

As alluded to in the previous paragraph, cross-stream POD modes were also created using the full range of image intensity (these are not included for brevity). These modes are similar to the modes of figure 12. The first 9 modes are largely focused on the periphery of the jet with nearly identical azimuthal character, i.e. the azimuthal mode number, n , is ± 1 , ± 2 , ± 3 , 0, ± 4 , respectively for the first 9 modes, while the higher-order full-intensity modes are more complex than the binary modes. As discussed in § 2.4, using the full-range of intensities was deemed unacceptable since the amount of jet/ambient air mixing that was required to obtain a pixel intensity of 0.4 (or any other threshold value) varied over the course of the data acquisition.

Therefore, pixels were defined as recording a ‘mixed’ or ‘unmixed’ state within the jet based upon a set threshold level.

Similar to the cross-stream POD modes of figure 12, the 16 streamwise POD modes shown in figure 13 have a distinct order. The first four modes consist of large oval-shaped features that span large streamwise distances, and are located within the outer region of the jet. In modes 1 and 2, these features have an asymmetric arrangement while mode 3 has a symmetric arrangement. Modes 5 and higher have features within the inner as well as outer regions of the jet. In modes 5 and 8, the modal composition is asymmetric while modes 9 and 12 are symmetric about the jet centreline. Modes 4 and 6 lack symmetry, which could be an experimental artefact, i.e. it is difficult to achieve exact symmetry in an experimental set-up. Many of the higher modes (8–16) have smaller features within the outer regions of the jet and are tilted, which is a common trait of large-scale structures subjected to a significant shear force (i.e. a shear layer). Mode 15 of the cross-stream POD consisted of a single feature at the jet centreline (figure 12), which is similar to POD mode 11 of the streamwise decomposition. As will be presented and discussed shortly, this POD mode seems to play a significant role in the noise-generation process.

The symmetric and asymmetric patterns that are present within these POD modes are impressive. It is known that axisymmetric jets possess various azimuthal modes (e.g. Freund & Colonius 2002). Instantaneous cross-stream images of the current jet show such azimuthal structures (Thurow *et al.* 2003). However, these structures are masked by the smaller scales in such a high-Reynolds-number jet. The POD technique itself acts as a filter to remove the smaller scales. In addition, the use of binary images is also expected to filter smaller scales. Therefore, it is conceivable that the small-scale filtering has brought out the large-scale azimuthal structures in this high-Reynolds-number high-speed jet. However, further experimental work is required to verify this finding.

We must remember that all the features within the POD modes and reconstructed images of § 3.4 are on a scale that is consistent with large-scale turbulence structures. None of them could be classified as small-scale since they are of the order of magnitude of the jet nozzle exit diameter, D . Truly small-scale turbulence structures are many orders of magnitude smaller than anything observed in the images from this high-Reynolds-number ($\sim 10^6$) jet. We should also understand that the large-scale structures of the jet are actually three-dimensional and extend beyond the two-dimensional plane of the flow images and POD modes. Freund & Colonius (2002) created a three-dimensional POD basis for a Mach 0.9 jet, and a few of the streamwise modes of figure 13 bear strong similarity to cross-sectional slices of their low-order axisymmetric and azimuthal pressure modes. Thus, it is probable that some of the POD features represent a single three-dimensional turbulence structure. This is a shortcoming that is being partially overcome by using two orthogonal visualization planes. Regardless, though, some aspects of the large structures are not captured.

3.3. NG and RQ selection criteria

As discussed, this work focuses on two ‘states’ of the jet (see figure 2). The first state is during the generation of large-amplitude acoustic events (noise generation, NG) while the second state is during extended periods that lack such sound generation (prolonged period of relative quiet, RQ). The NG image sets (one set for the cross-stream and another for the streamwise) were chosen based on the microphone array indicating that a flow image had been taken during the generation of a large-amplitude acoustic event. For both laser sheets, determination of which images will be included

in the NG data sets relies on knowledge of when and where the large-amplitude events originated within the jet (four-dimensional, space–time, noise source localization). The RQ image sets (again one set for the cross-stream and another for the streamwise) relied on the retarded time for an acoustic wave and the duration of the period of relative quiet.

Images within the NG data sets had acoustic data that met four criteria in the source location and emission time for the large-amplitude sound event. The first criterion was on the x -location of the source. For the cross-stream image set, the source of the event had to be located within $1x/D$ of the illumination plane (i.e. between 8 and $10x/D$); while for the streamwise image set, the source had to be between 7 and $11x/D$. This ensured the sound source was captured within the flow image. The second criterion was on the z -location of the source. For both image sets, the source had to be located above the jet centreline as determined by both the three-dimensional noise source location calculation and a phase-lag measurement between the top front and bottom front microphones. Such a limitation on the z -location minimized the impact of refraction on the noise source location procedure. The third criterion was on the timing of the event reaching the two sides of the microphone array. The bottom front microphone had to record a similar-sign large-amplitude event within 1 convective time scale ($t^* u_c/D$) of the large-amplitude event being recorded by the top microphone. This requirement ensured the sound wave radiated relatively uniformly over all azimuthal directions, and it reduced the likelihood of refraction influencing the noise source computation. The fourth and final criterion was on the timing of the large-amplitude acoustic event generation relative to the moment of flow illumination. For the cross-stream image set, the time lag between generation and illumination had to be under 0.5 convective time scale. This ensured that the image captured the jet shortly before or after the emission of the large-amplitude event. There were 200 cross-stream images that met the above criteria. Since the streamwise images were taken in temporally resolved sets of 16 useful images with $6\ \mu\text{s}$ separation, there were a large number of images available. Through phase alignment of the images relative to the moment of noise emission (estimated generation time for the large-amplitude event), a time series was created showing the mixing-layer evolution (and therefore the evolution of the large-scale turbulence structures) within the region where acoustic events were generated. A series of pseudo phase-locked data consisting of 134 time steps separated by $6\ \mu\text{s}$ was created. It consisted of $402\ \mu\text{s}$ surrounding the estimated moment of peak acoustic energy generation. This is about four convective time scales. Each time step was comprised of approximately 180 images. Two and a half convective time scales of data will be presented in the next section with 0.13 convective time scale ($12\ \mu\text{s}$) separation while the entire data set can be found in Hileman (2004).

Images within the RQ data sets had acoustic data from both the top and bottom front microphones that lacked any acoustic emission over 1.5σ for a set time period. At a minimum, the time period of both the top and bottom front microphones included 5 convective time scales that were centred on the retarded time for a sound wave to reach the array from the jet centreline (as measured relative to the flow imaging). In other words, the acoustic signature did not exceed 1.5σ between 3.1 and 3.6 ms after the flow image was captured with flow visualization. All time signatures that met this criterion were gathered with the duration of their quiet period. To match the number of images within the NG cross-stream image set, the 200 longest periods of relative quiet were used to compile the RQ cross-stream image set. Similarly, the 180 longest periods of relative quiet were used to compile the RQ streamwise image set. The shortest of these relative quiet periods was 13 convective time scales in duration

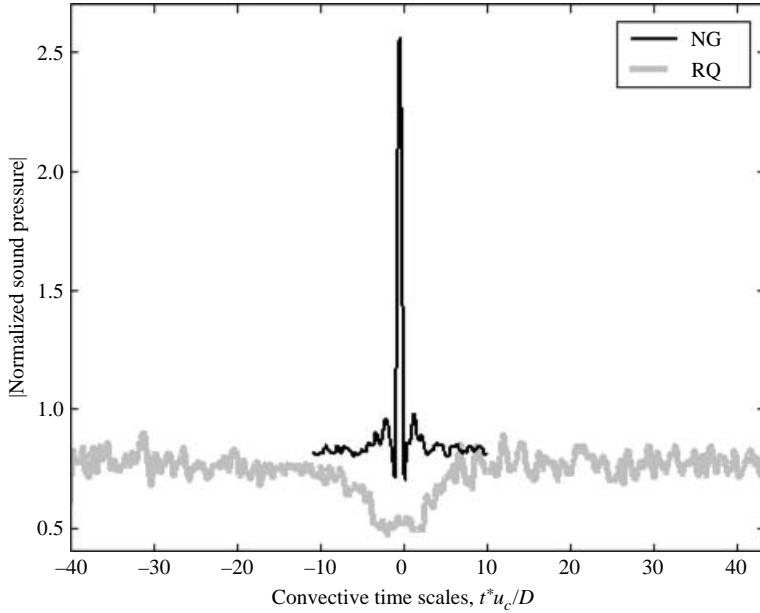


FIGURE 14. Absolute value of normalized sound pressure from ensemble-averaged noise generation (NG) events and from periods that lack noise generation (RQ) at the microphone array.

and the longest was 29 convective time scales. The streamwise RQ image set actually consisted of 180 sets of 16 flow images where each image set spanned $90\mu\text{s}$ (0.94 convective time scales). They were not phase-locked since there is no phase-defining event.

The magnitude of the normalized sound pressure data for the streamwise NG and RQ data sets are presented in figure 14. The average NG acoustic data was created from 2 ms of data over the 1846 acoustic events, while that of the RQ was created from the 180 sets of acoustic data. The plots show data from the top front microphone (microphone 2 of figure 3). Although not shown here, the bottom front microphone data were similar (Hileman 2004). The NG data set has a large peak while the RQ data set has a distinct ‘well’ of reduced sound pressure. The 5 convective time scale range that was required to be considered a relative quiet period is visible within the figure. The gradual increase on either side shows the varied lengths of relative quiet among the RQ acoustic signatures.

3.4. Image reconstruction

The POD modes were used as a basis that describes the shape, size and spatial distribution of the significant features of the jet. With these modes and a judicious selection of weightings (time coefficients), we could reconstruct a typical image of the jet to a reasonable approximation. To test the accuracy of the reconstructions, the modes of figure 12 were used to create 24 time coefficients (one for each mode) for a few sample flow images. These coefficients were then combined with the modes to yield reconstructed flow images. The error between the original binary flow images and the reconstructed images was $\sim 20\%$, while the error between the original full intensity scale flow images and the reconstructed images was $\sim 40\%$.

With the POD modal basis, the POD time coefficients were determined for every image within the NG and RQ image sets along with a randomly selected image set. For the cross-stream cases, 24 time coefficients were determined for each image since there were 24 POD modes, while the streamwise images had 16 time coefficients for the 16 POD modes. For the POD modes, the positive or negative sign of the structure only has significance within any individual mode (e.g. to determine asymmetry *vs.* symmetry). The sign of one mode is irrelevant to another mode. However, in modal reconstructions, the sign is quite important. The sign of a reconstructed image shows the deviation from the image mean. Lighter regions have greater than average intensity (increased entrainment and mixing, i.e. presence of large-scale structures within the mixing layer) while darker regions have lower than average intensity (corresponds to a lack of mixing and large-scale structures). These time coefficients could then be averaged across the entire data set to yield a representative coefficient for each POD mode. The average time coefficients may not mean much since the jet mixing layer is constructed from a combination of multiple POD modes. Instead of comparing the average time coefficient for each mode individually, they were combined to reconstruct the jet. The procedure is straightforward: the average time coefficient was used as a weighting factor for each mode and the weighted modes were combined to reconstruct the jet. The coefficients of the individual modes can be found in Hileman (2004).

The cross-stream reconstructed images are shown in figure 15. All of these reconstructed images are plotted with the same intensity contours. Figure 15(a) shows the reconstructed images using all 24 modes. The reconstructed RQ image is dominated by relatively large features around the periphery of the jet. This is in contrast to the reconstructed NG image, which consists of many smaller features that span the entire cross-section of the jet. The random reconstructed image seems to be a combination of the NG and RQ, as we would expect. There is a difference between the RQ and NG states, based on both feature size and distribution. Figure 15(b) shows the reconstructed jet using the first 11 modes (see figure 12), which are dominated by relatively large features that are on the periphery of the jet. The reconstructed RQ image (using modes 1–11) shows features similar to those constructed using modes 1–24, indicating these lower-order modes dominate during relative quiet periods. This is in distinct contrast to the average reconstructed NG image, which bears little resemblance to that created with all 24 modes. Figure 15(c) shows the reconstructed images using modes 12 to 24, which consisted of smaller features that spanned the entire jet cross-section. The reconstructed RQ image has alternating positive and negative fluctuating features (negative on the outside) with a lack of any feature at the jet's centre. The reconstructed NG image also has alternating positive and negative fluctuating features on the jet's periphery, but the positive fluctuations are now on the outer regions. More significantly, there is a strong, positive fluctuation at the jet's centre that was not present in the RQ reconstructions. Thus, during noise generation, the jet was dominated by many relatively small alternating features that surround a large feature at the jet centreline. This feature is absent from reconstructed images of relative quiet periods. In Hileman (2004), 400 NG and RQ data sets were also used for reconstruction. With the additional images, larger time lags were included in the NG data set, and shorter periods of relative quiet were included in the RQ data set. Many of the trends observed in figure 15 were repeated with these larger data sets. The striking aspect of these reconstructed images lies on the jet centreline. The RQ case has a region of negative fluctuation at the jet's centre while the NG case has a corresponding region of positive fluctuation.

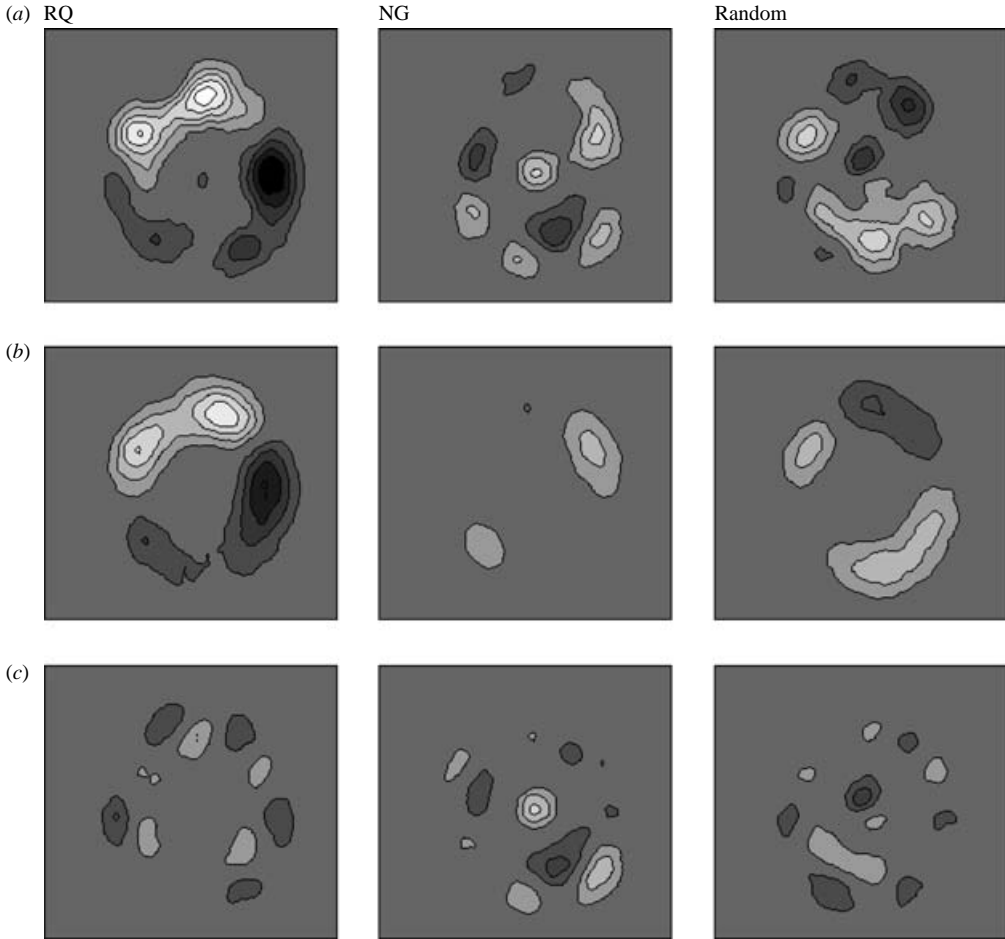


FIGURE 15. Average of 200 reconstructed images from the sorted RQ, sorted NG, and random sets of cross-stream flow images. Three sets of POD modes were used in the reconstruction: (a) 1–24 (all), (b) modes 1–11 and (c) modes 12–24.

Because of their temporal resolution, the reconstructions of the streamwise NG and RQ image sets can be used to analyse the evolution of the jet and the large-scale turbulence structures that comprise it. All 16 streamwise POD modes (see figure 13) were used to create the temporally resolved reconstructed RQ image set shown in figure 16. The same 16 modes were used to reconstruct 20 time steps ($228\ \mu\text{s}$ or ~ 2.5 convective time scales) that are crudely phase-locked to the moment of noise generation for the NG data set in figure 17. Time zero is the estimated moment of sound emission. The reconstructed images are quite rich and complex in detail. There are significant differences between the two jet ‘states’ that are consistent with the cross-stream reconstructions. To understand these differences better, the two sets of images were reconstructed using modes that dominate the outer part of the jet (modes 1–4) and those spanning the entire cross-section of the jet (modes 5–16). This is similar to the manner used in the analysis of the cross-stream visualization plane in figure 15. The temporally resolved reconstructed image sets that were created from the first four modes are given in figure 18 (reconstructed RQ image set) and figure 19 (reconstructed NG image set). With only four modes, the reconstructed

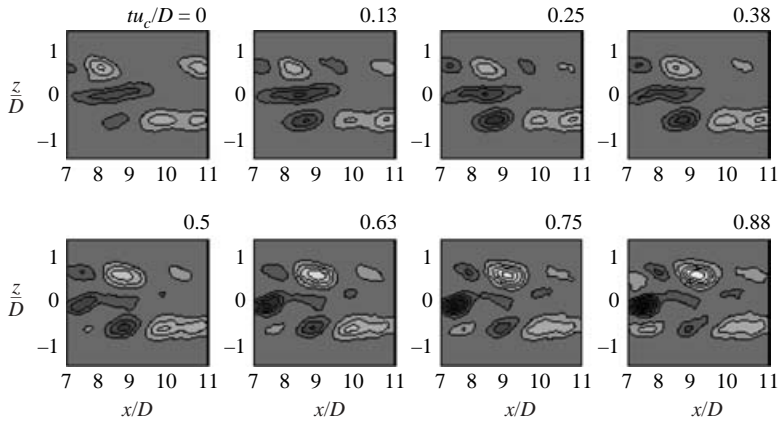


FIGURE 16. Reconstructed images for streamwise RQ state using modes 1 to 16.

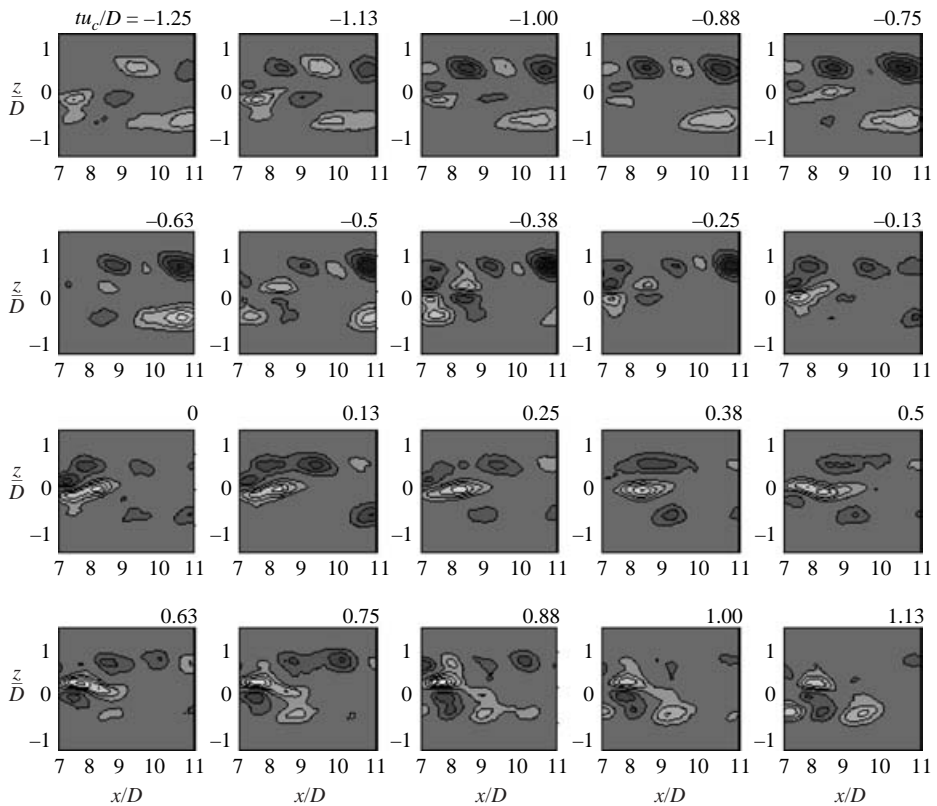


FIGURE 17. Reconstructed images for streamwise NG state using modes 1 to 16.

RQ image set has large features possessing strong, positive fluctuations while the reconstructed NG image set has spatially large, but negative fluctuation features for 0.4 convective time scales on either side of the estimated time of noise emission ($t^* u_c/D = 0$). At the moment of noise emission, there is actually a lack of any features (positive or negative), which is in agreement with the reconstructed image of the cross-stream plane using the lower POD modes (see reconstructed NG images of

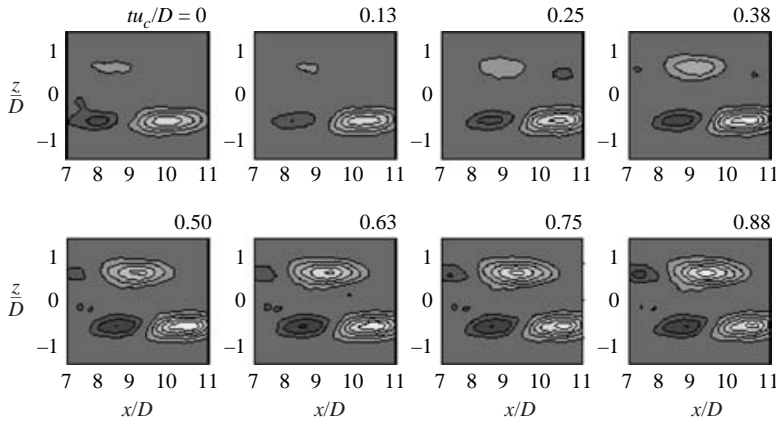


FIGURE 18. Reconstructed images for streamwise RQ state using modes 1 to 4.

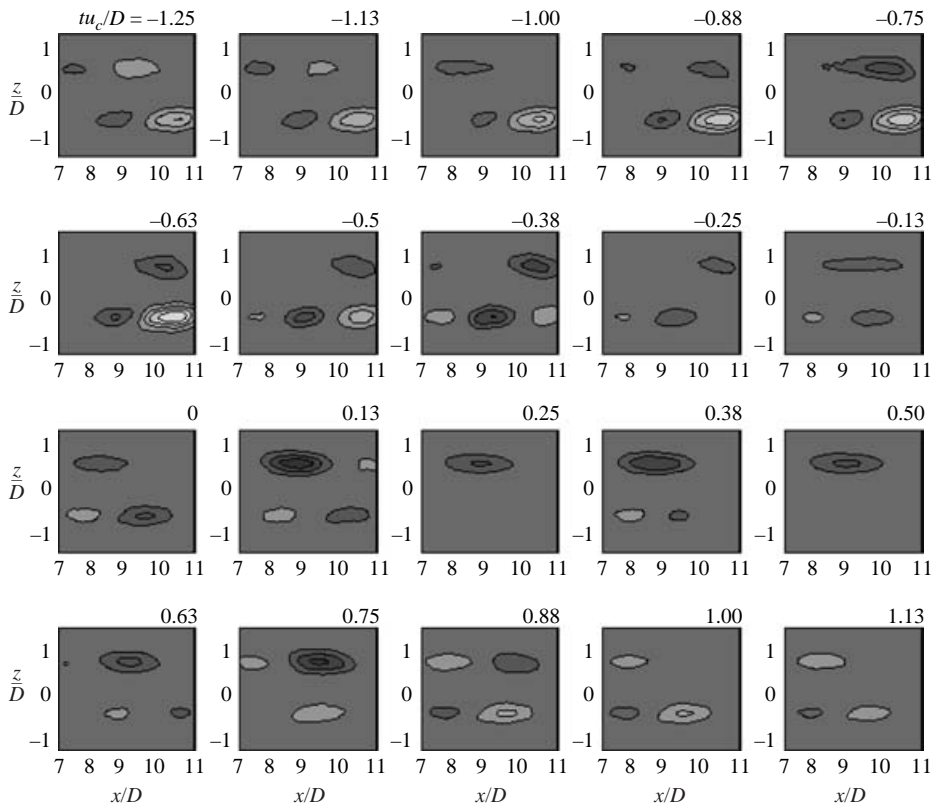


FIGURE 19. Reconstructed images for streamwise NG state using modes 1 to 4.

figure 15 using modes 1 to 11 of figure 12). The streamwise, reconstructed RQ image set matches the cross-stream reconstructed RQ image in both the size and the sign of the features that dominate. In both cases, a positive (white) region is located above the jet centreline whereas a negative (black) region is below. The result becomes even more impressive if we consider that the cross-stream and streamwise reconstructed images were created from flow images taken with two independent and quite different

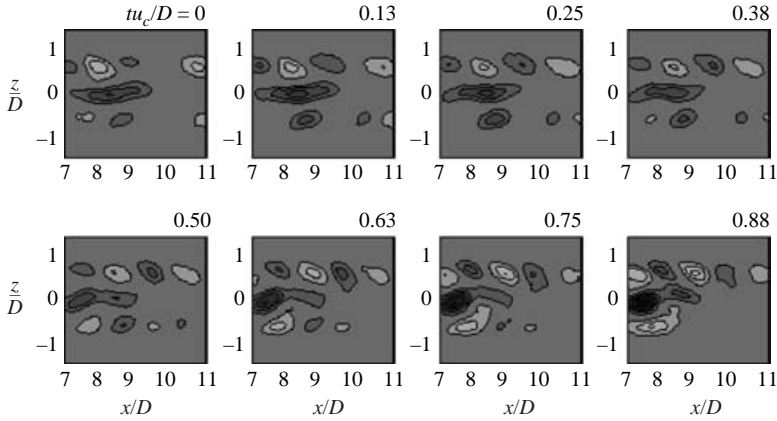


FIGURE 20. Reconstructed images for streamwise RQ state using modes 5 to 16.

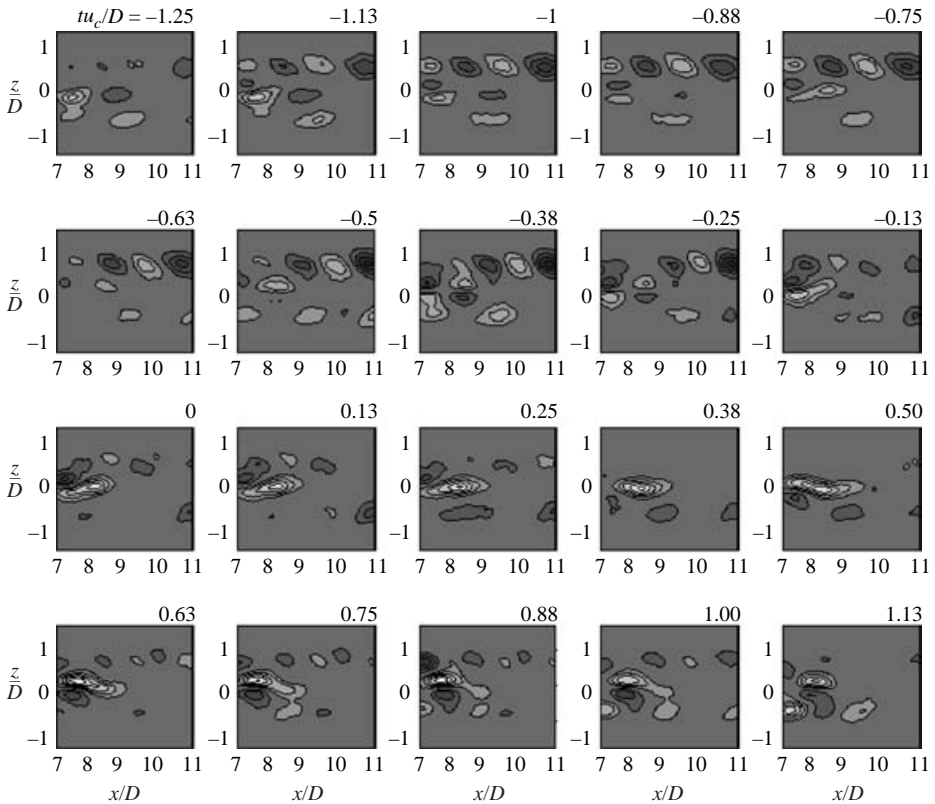


FIGURE 21. Reconstructed images for streamwise NG state using modes 5 to 16.

laser-camera systems and when combined they give a pseudo three-dimensional view of the jet mixing layer.

The streamwise reconstructed RQ and NG images using modes 5 to 16 (figures 20 and 21, respectively) also corroborate the findings of the cross-stream plane while adding to our knowledge of jet noise emission. The reconstructed RQ images have a negative fluctuation region along the jet centreline over the duration of the image set

while the reconstructed NG image set has a corresponding dominant positive fluctuation region for times between -0.13 and $+0.5$ convective time scales. Before the noise emission time ($-1.13 < t^*u_c/D < -0.25$ of the reconstructed NG image set), a series of alternating sign features forms, tilts and disintegrates within the top half of the mixing layer. During the last stages of their existence ($-0.25 < t^*u_c/D < 0$), the alternating flow features are replaced by a region of positive centreline intensity (between 7 and $9x/D$). This feature is alone on the jet centreline for quite some time. The large robust flow features in the top half of the mixing layer apparently are involved with entraining large quantities of ambient air into the jet as evidenced by the increased jet centreline intensity. The formation and disintegration of alternating flow features within the top half of the mixing layer bears an uncanny similarity to a process hypothesized in Morrison & McLaughlin (1979). They conjectured that the majority of the noise within a low-Reynolds-number (3700) Mach 1.4 jet is due to the rapid decay (disintegration) of instability waves within the jet, and this disintegration involves a ‘relatively violent fluid dynamic action’ Immediately downstream of the end of the potential core (where the acoustic waves of their jet originated), they found the coherence of the velocity fluctuations from hot-wire measurements decreased dramatically. Based on these observations, they conjectured that the majority of the noise was due to the rapid decay (disintegration) of the instability waves. The temporally resolved image set shown in figure 21 is the first to capture this noise generating ‘fluid dynamic action’ in a high-Reynolds-number jet.

Freund & Colonius (2002) created POD modes for a Mach 0.9 jet simulation using a variety of near-field norms (pressure, velocity, turbulent kinetic energy within the jet) as well as the far-field sound pressure. They selected near-field quantities for optimization of the modal basis, but also computed the sound pressure of the far acoustic field. Through this procedure they found that the near-field POD norms captured only a small fraction of the far-field sound field. They also selected the far-field pressure for optimization and computed the near-field pressure. This is similar to the process used herein for NG image set analysis since both rely on far-field sound pressure measurements to determine the near-field features that coincide with sound generation. They found the reduced near-field pressure had an abrupt change in structure near the end of the potential core, which was unlike the most energetic near-field pressure modes with their regular structure. These results further corroborate the instability wave disintegration observed here.

3.5. Discussion

The results of § 3.1 comparing the mean noise source region to statistical flow images of the jet showed the dominant sound was emanating from a region dominated by the interaction of the two sides of the mixing layer around the jet potential core end. In the reconstructed NG images in both the cross-stream and streamwise planes, there was a positive intensity fluctuation at the centreline. Apparently, this is a key aspect of noise generation. Within the RQ images, there was either a corresponding negative fluctuation in the same location (streamwise image) or no fluctuation at all (cross-stream image). The region of the fluctuation is along the centreline and downstream of the end of the potential core where the velocity decreases from the exit value. When there is a positive fluctuation, the unmixed core of the jet is shorter than its average (the opposite is true for a negative fluctuation or no fluctuation). Thus, during the emission of large-amplitude acoustic events, the unmixed core of the jet was considerably shortened compared to that of the extended periods that lacked such acoustic emission (in the direction of the microphone array). This observation is consistent

with the subjective interpretations of the simultaneous data presented in Hileman & Samimy (2001) and Hileman *et al.* (2002). Those works suggested one of the mechanisms of noise emission was the interaction of large-scale structures across the two sides of the mixing layer (a process that would lead to a shortening of the unmixed jet core). Such interaction invariably leads to mixed fluid reaching the core of the jet.

Another stark contrast between the two states (NG versus RQ) is the scales of their dominant features. The cross-stream image of the RQ state could largely be reconstructed by the lower-order modes or large-flow features. In both the RQ and NG streamwise reconstructions, the large features of the lower-order modes seem to be benign with little change over the duration of either temporally resolved image set. The cross-stream image of the NG state could be reconstructed from the higher-order modes that emphasized the entire jet width while the streamwise NG reconstructions consisted of the formation and destruction of the wavelike flow features in the upper half of the mixing layer. Apparently, during noise generation, there are more interactions between rapidly evolving and relatively smaller large-scale turbulence structures than the larger but benign structures that are prevalent during periods of relative quiet. These findings suggest the largest features of the jet are not directly responsible for noise generation, but it is the interaction of relatively smaller features that are critical to sound generation.

The phase-locked, streamwise NG reconstructed images showed how these smaller (but still large-scale) flow features interact prior to noise emission. A series of alternating flow features persisted for about one convective time scale before abruptly disintegrating shortly before the moment of sound emission. Prior to their breakdown, the features tilted dramatically. Apparently, noise generation within the high-Reynolds-number Mach 1.28 jet is dominated by a set of relatively small features (but still of the order of a fraction of a nozzle exit diameter) that entrain fluid into its centre and in the process change dramatically in appearance. These observations are in general agreement with the low-Reynolds-number work discussed in § 1, but it is the first time they have been visualized from a statistically significant data set in a high-speed flow.

We must remember, though, that these modes are fluctuations from the mean image. The large-scale structure interaction that is being represented by this wavelike flow feature might take the form of the ‘tilt-stretch-tear-pair’ observed by Thurow *et al.* (2003) since those images were taken of the same jet that is being examined here. In the works leading up to this (Hileman & Samimy 2001; & Hileman *et al.* 2002), large-scale structure roll-up and large-scale structure tearing were both observed on the microphone side of the mixing layer in the regions of noise generation. Thus, one (or both) of these might also be represented by the formation and destruction of the wavelike flow features. Even those who might find the subjective interpretations of this section less than desirable would agree that there are potentially several mechanisms that are responsible for the generation of noise; hence, the reconstructions are probably averaging/combining the mechanisms of sound generation by large-scale turbulence structures.

Ffowcs Williams & Kempton (1978) compared two analytical models (instability wave and vortex pairing) for noise generation from large-scale structures in a jet. Their instability wave model has a sinusoidal growth that leads to a ‘break’ point that is followed by equal sinusoidal decay. As shown in figure 21, the flow features that comprise the instability wave remain unchanged from -1.13 to -0.5 convective time scales. At $t^*u_c/D = 0.38$, the wave changes appearance (i.e. ‘breaks’) with a series of alternating features forming on the bottom side of the instability wave between 7 and $10x/D$. Change occurs rapidly and by the estimated moment of noise emission ($t^*u_c/D = 0$), the three pairs of opposite-signed large features that had been on the

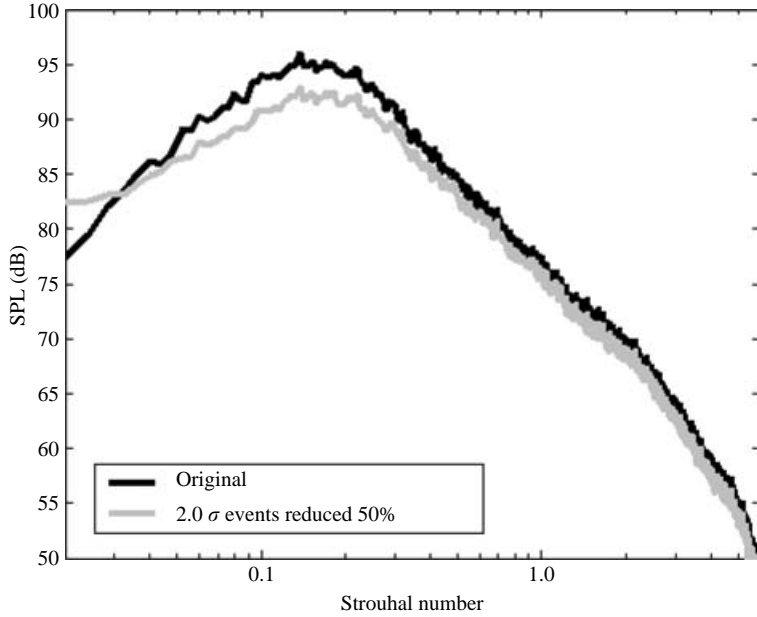


FIGURE 22. Potential noise reduction for the Mach 1.3 jet at $\theta = 30$ if the amplitude of the large-amplitude acoustic events were reduced by 50 %.

upper and lower sides of the mixing layer between 7 and $10x/D$ have been replaced by a single positive fluctuation feature at the jet’s core (between 7 and $9x/D$). This observed development is not symmetric in time. Instead, the instability wave ends quite abruptly. Based on these results, the noise production process seems to be best modelled with an instability wave having an abrupt disintegration after the ‘break’ (i.e. a truncated instability wave, Kastner *et al.* 2005). We speculate that the disintegration is caused by the dynamic interaction of large-scale structures that leads to large fluid entrainment to the jet core.

As to the question of how to make jet engines quieter, the reconstructed images for the relatively quiet case have a well-defined unmixed core as shown by the negative intensity fluctuations at the jet centreline. This is opposite to the NG reconstructed images. Although not shown here, the unmixed cores of the ten longest RQ image sets move in a wavelike motion with large structures surrounding (Hileman 2004). This rotation of the unmixed core of the jet was captured by Thurow *et al.* (2003) in a time-resolved flow movie of this jet at a cross-stream location of $6x/D$. Based on these results, noise reduction might be achieved by promoting the growth of large-scale structures that rotate around the jet centreline (a helical mode) where the unmixed potential core of the jet is stretched as far downstream as possible. Such a jet would inhibit the interaction of the large structures by maintaining a buffer between them, and the energy that is contained within them would be dissipated by their gradual disintegration instead of the abrupt changes observed in figure 21. Of course, this noise reduction scheme is only a conjecture at this point. If such a jet modification succeeded in changing the large-event amplitude, then what level of noise reduction could be expected? To make an estimate, we need only set all of the acoustic events that were above 2.0σ (and the acoustic data immediately surrounding its peak) to some percentage of their original value and then convert the data to the frequency domain. As shown by figure 22, if we could reduce the magnitude of all

large-amplitude events by 50 %, then the SPL drops by more than 3 dB at the peak Strouhal number of the 30° location.

4. Concluding remarks

This work was devoted to relating sound production to the evolution and interaction of large-scale turbulence structures within an axisymmetric jet. This was conducted in a rather unorthodox fashion by determining the four-dimensional source of the large-amplitude acoustic events within the time domain for their source and then examining flow images taken of the source region. For this reason, established experimental methods were modified as discussed in §2. The focus was on a Mach 1.28 jet owing to the ease of flow visualization and the similarity of its large-scale structure dynamics from a compressibility viewpoint to a heated Mach 0.9 jet. One of these techniques involved a novel microphone arrangement and algorithm for noise source localization that was used to create a frequency-streamwise source location distribution that agreed well with the results of previous workers using a variety of source localization techniques (figure 7). The regions of noise generation coincide with the location where the sides of the mixing layer merge.

There is a distinct difference in the structure of the jet during the time preceding and following large-amplitude noise generation compared to periods that lack noise generation. This difference was observed through a novel approach where the origins of large-amplitude sound events were correlated to simultaneously acquired temporally resolved flow images. To ensure statistical viability of the results, a large set of simultaneous flow and acoustic data was acquired consisting of microphone array measurements and flow images on two planes that were centred on the region of maximum noise source concentration ($9x/D$). The images were decomposed using the POD technique to extract a basis of the relative size and position of the large-scale structures. The symmetry of the POD modes was impressive as they were easily grouped into those that emphasize features on the periphery of the jet and those that emphasize features spanning the entire jet cross-section. Two contrasting jet states were examined with the modal basis: (i) images that were obtained during intense noise generation processes (NG) and (ii) those that were acquired while the acoustic array recorded a prolonged period of relative quiet (RQ). The dramatic difference in the far-field acoustic signatures of these sets was shown in figure 14. Images were reconstructed using POD modes that focused on flow features that were located either on the periphery of or spanned the width of the jet to create cross-stream and streamwise images that showed the differences between the NG and RQ states. Consistent with the rapid changes observed in the region of noise generation in low-Reynolds-number jets by Freund (2001) and Morrison & McLaughlin (1979), a series of robust flow features appeared one convective time scale before noise emission and then rapidly disintegrated immediately before noise emission. Coincident with the disintegration, a positive intensity fluctuation formed at the jet centreline in a region that is immediately past the end of the potential core (the robust flow features, consistent with large-scale turbulence structures, apparently entrain ambient fluid into the jet). This is consistent with a shortening of the unmixed core of the jet from the mean. These results showed the features of an evolving jet (and the underlying large-scale turbulence structures) that are responsible for noise generation within a high-speed high-Reynolds-number jet. They were then contrasted with the data of the RQ state, which had a significantly extended unmixed core region. The discussion of §3.5 elaborated on meaning behind these findings.

Further aeroacoustics work should be conducted using the techniques outlined in this work. Within a number of years, the flow-visualization aspect of the simultaneous flow and acoustic measurements could be replaced with temporally resolved planar velocimetry (e.g. Thurow 2005) and the image intensity of the POD modes will be replaced by time-dependent quantitative turbulence measurements of velocity fluctuations and vorticity measurements. At that point, much new knowledge will be made available. However, these techniques should not lie idle until then. The outlined technique could easily be applied to any number of existing DNS or LES databases. Measurement points can be established in the computational far field and then the microphone array procedure could be used to locate the sound sources within the simulated flow in four-dimensional space–time. With knowledge of where and when each sound wave was produced, the regions of noise generation could be examined over several convective time scales prior to and following the moment of noise emission. With a numerical database, many turbulence quantities (e.g. Reynolds stress) could be computed in three-dimensions for the flow field. The POD technique could then be used to decompose the flow field and modal reconstruction used to establish a low-order model of the flow. Many cases could be considered including axisymmetric and asymmetric sound generation as well as extended periods where the measurement points recorded lower sound pressure levels. The asymmetric case was observed in Hileman *et al.* (2002) and it could yield insight into means of using the turbulence within the jet to shield acoustic radiation that is radiated by other regions of the mixing layer. Through such analysis, we might be able to determine quantitatively the process of sound generation by large-scale turbulence.

This work was sponsored by the Air Force Office of Scientific Research with Drs John Schmisser and Steven Walker as the Technical Monitors. J. I. H., B. S. T. and E. J. C. would like to thank the Ohio Space Grant Consortium, the Department of Defense (NDSEG and DAGSI) for their respective doctoral fellowships.

REFERENCES

- AHUJA, K. K., MASSEY, K. C. & D'AGOSTINO, M. S. 1998 A simple technique of locating noise sources of a jet under simulated forward motion. *AIAA Paper* 98-2359.
- BROWN, G. L. & ROSHKO, A. 1974 On density effects and large structure in turbulent mixing layers. *J. Fluid Mech.* **64**, 715–816.
- CARABALLO, E., SAMIMY, M., SCOTT, J., NARAYANAN, S. & DEBONIS, J. 2003 Application of proper orthogonal decomposition to a supersonic axisymmetric jet. *AIAA J.* **41**, 866–877.
- CHU, W. T., LAUFER, J. & KAO, K. 1972 Noise source distributions in subsonic jets. *Inter-Noise 72*, Inst. of Noise Control Engineering of the USA, Washington, DC.
- CITRINITI, J. & GEORGE, W. 2000 Reconstruction of the global velocity field in the axisymmetric mixing layer utilizing the proper orthogonal decomposition. *J. Fluid Mech.* **418**, 137–166.
- CRIGHTON, D. G. 1975 Basic principles of aerodynamic noise generation. *Prog. Aerospace Sci.* **16**, 31–96.
- CROW, S. C. & CHAMPAGNE, F. H. 1971 Orderly structure in jet turbulence. *J. Fluid Mech.* **48**, 547–591.
- FFOWCS WILLIAMS, J. E. 1963 The noise from turbulence convected at high speed. *Phil. Trans. R Soc. Lond. A* **255**, 469–503.
- FFOWCS WILLIAMS, J. E. & KEMPTON, A. J. 1978 The noise from the large-scale structure of a jet. *J. Fluid Mech.* **84**, 673–694.
- FISHER, M. J., HARPER-BOURNE, M. & GLEGG, S. A. L. 1977 Jet engine source location: the polar correlation technique. *J. Sound Vib.* **51**, 23–54.
- FREUND, J. 2001 Noise sources in a low-Reynolds-number turbulent jet at Mach 0.9. *J. Fluid Mech.* **438**, 277–305.

- FREUND, J. & COLONIUS, T. 2002 POD Analysis of Sound Generation by a Turbulent Jet. *AIAA Paper* 2002-0072.
- GROSCHKE, F. R. 1973 Distributions of sound source intensities in subsonic and supersonic jets. *AGARD CP* 31, paper 4.
- HERNAN, M. A. & JIMENEZ, J. 1982. Computer analysis of a high-speed film of the plane turbulent mixing layer. *J. Fluid Mech.* **119**, 323–345.
- HILEMAN, J. 2004 *Large-Scale Structures and Noise Generation in High-Speed Jets*. PhD Dissertation, The Ohio State University Department of Mechanical Engineering.
- HILEMAN, J. & SAMIMY, M. 2001 Turbulence structures and the acoustic far-field of a Mach 1.3 jet. *AIAA J.* **39**, 1716–1727.
- HILEMAN, J. & SAMIMY, M. 2003 Effects of vortex generating tabs on noise sources in an ideally expanded Mach 1.3 jet. *Intl J. Aeroacoust.* **2**, 35–63.
- HILEMAN, J., THUROW, B. & SAMIMY, M. 2002 Exploring noise sources using simultaneous acoustic measurements and real-time flow visualizations in jets. *AIAA J.* **40**, 2382–2392.
- HILEMAN, J., THUROW, B. & SAMIMY, M. 2004 Development and evaluation of a 3-D microphone array to locate individual acoustic sources in a high-speed jet. *J. Sound Vib.* **276**, 649–669.
- HUSSAIN, A. K. M. F. & CLARK, A. R. 1981 On the coherent structure of the axisymmetric mixing layer: a flow-visualization study. *J. Fluid Mech.* **104**, 263–294.
- KASTNER, J., HILEMAN, J. & SAMIMY, M. 2004 Exploring high-speed axisymmetric jet noise control using Hartmann tube fluidic actuators. *AIAA Paper* 2004-0186.
- KASTNER, J., SAMIMY, M., HILEMAN, J. & FREUND, J. 2005 Comparison of noise sources in high and low Reynolds number high-speed jets. *AIAA Paper* 2005-3092.
- KERECHANIN, C. W., SAMIMY, M. & KIM, J.-H. 2001 Effects of nozzle trailing edges on acoustic field of supersonic rectangular jet. *AIAA J.* **39**, 1065–1070.
- LEE, H. K. & RIBNER, H. S. 1972 Direct correlation of noise and flow of a jet. *J. Acoust. Soc. Am.* **52**, 1280–1290.
- LIGHTHILL, M. J. 1952 On sound generated aerodynamically: I. General theory. *Proc. R. Soc. Lond. A* **211**, 564–581.
- LILLEY, G. M. 1991 Jet noise classical theory and experiments. In *Aeroacoustics of Flight Vehicles: Theory and Practice*, vol. 1 (ed. H. H. Hubbard). NASA RP-1258.
- LUMLEY, J. 1967 The structure of inhomogeneous turbulent flows. In *Atmospheric Turbulence and Wave Propagation* (ed. A. M. Yaglow & V. I. Tatarski) pp. 166–176. Nauka, Moscow.
- MORRISON, G. L. & McLAUGHLIN, D. K. 1979 Noise generation by instabilities in low Reynolds number supersonic jets. *J. Sound Vib.* **65**, 177–191.
- MURAKAMI, E. & PAPAMOSCHOU, D. 2000 Eddy convection in coaxial supersonic jets. *AIAA J.* **38**, 628–635.
- NARAYANAN, S., BARBER, T. J. & POLAK, D. R. 2002 High subsonic experiments: turbulence and noise generation studies. *AIAA J.* **40**, 430–437.
- PANDA, J. & SEASHOLTZ, R. G. 2002 Experimental investigation of density fluctuations in high-speed jets and correlation with generated noise. *J. Fluid Mech.* **450**, 97–130.
- PAPAMOSCHOU, D. & ROSHKO, A. 1988 The compressible turbulent mixing layer: an experimental study. *J. Fluid Mech.* **197**, 453–477.
- SAMIMY, M., ZAMAN, K. B. M. Q. & REEDER, M. 1993 Effect of tabs on the flow and noise field of an axisymmetric jet. *AIAA J.* **31**, 609–619.
- SAROHIA, V. & MASSIER, P. F. 1977 Experimental results of large-scale structures in jet flows and their relation to jet noise production. *AIAA Paper* 77-1350.
- SCHAFFAR, M. 1979 Direct measurements of the correlation between axial in-jet velocity fluctuations and far-field noise near the axis of a cold jet. *J. Sound Vib.* **64**, 73–83.
- SIDDON, J. E. 1973 On noise mechanisms. Noise source diagnostics using causality correlation. *AGARD CP* 131.
- SIMONICH, J., NARAYANAN, S., BARBER, T. J. & NISHIMURA, M. 2001 Aeroacoustic characterization, noise reduction and dimensional scaling effects of high subsonic jets. *AIAA J.* **39**, 2062–2069.
- SIROVICH, L. 1987 Turbulence and the dynamics of coherent structures, Part I: coherent structures. *Q. Appl. Maths* **45**, 561–571.
- STROMBERG, J. L., McLAUGHLIN, D. K. & TROUTT, T. R. 1980 Flow field and acoustic properties of a Mach number 0.9 jet at a low Reynolds number. *J. Sound Vib.* **72**, 159–176.

- TAM, C. K. W. 1991 Jet noise generated by large-scale coherent motion. In *Aeroacoustics of Flight Vehicles: Theory and Practice*, vol. 1 (ed. H. H. Hubbard). NASA RP-1258.
- TAM, C. K. W. 1998 Jet noise: since 1952. *Theoret. Comput. Fluid Dyn.* **10**, 393–405.
- TAM, C. K. W., GOLEBIOWSKI, M. & SEINER, J. M. 1996 On the two components of turbulent mixing noise from supersonic jets. *AIAA Paper* 96-1716.
- TAM, C. K. W. & ZAMAN, K. B. M. 2000 Subsonic jet noise from nonaxisymmetric and tabbed nozzles. *AIAA J.* **38**, 592–599.
- THUROW, B. 2005 *On the convective velocity of large-scale structures in compressible axisymmetric jets*. PhD dissertation, The Ohio State University Department of Mechanical Engineering.
- THUROW, B., HILEMAN, J., SAMIMY, M. & LEMPERT, W. 2002 A technique for real-time visualization of flow structure in high-speed flows. *Phys. Fluids* **14**, 3449–3452.
- THUROW, B., SAMIMY, M. & LEMPERT, W. 2003 Compressibility effects on turbulence structures of axisymmetric mixing layers. *Phys. Fluids* **15**, 1755–1765.
- UKEILEY, L. & SEINER, J. 1998 Examination of large-scale structures in a transonic jet mixing layer. *ASME FEDSM* 98-5234.
- VENKATESH, S. R., POLAK, D. R. & NARAYANAN, S. 2003 Beamforming algorithm for distributed noise source localization and its application to jet noise. *AIAA J.* **41**, 1238–1246.
- ZAMAN, K. B. M. Q., REEDER, M. F. & SAMIMY, M. 1994 Control of an axisymmetric jet using vortex generators. *Phys. Fluids* **6**, 778–793.